The Thesis Committee for Lucas Ryan Shearer
certifies that this is the approved version of the following thesis:

Marine Sediment Characterization Through Echo Sounder Measurement Analysis

APPROVED BY

SUPERVISING COMMITTEE:

Mark F. Hamilton, Supervisor

Aaron M. Gunderson, Co-Supervisor

Marcia J. Isakson

Marine Sediment Characterization Through Echo Sounder Measurement Analysis

by

Lucas Ryan Shearer

THESIS

Presented to the Faculty of the Graduate School of

The University of Texas at Austin

in Partial Fulfillment

of the Requirements

for the Degree of

MASTER OF SCIENCE IN ENGINEERING

THE UNIVERSITY OF TEXAS AT AUSTIN

May 2020

For Al and Jo

Acknowledgments

I would like to thank and acknowledge my academic and research advisors, Dr. Mark Hamilton, Dr. Aaron Gunderson, and Dr. Marcia Isakson, for their guidance both in the classroom and in the laboratory. I would like to thank all individuals, listed or not, which were involved in the collection and analysis of the experimental data referenced herein: Dr. Preston Wilson, Dr. Megan Ballard, Dr. Jason Sagers, Dr. Gabriel Venegas, Justin Dubin, Dr. Marcia Isakson, Michael Rukavina, Ricky Lenhart, Johanna Owens, Emery Stokes, the Dauphin Island Sea Laboratory personnel, and all of the research vessel crews. I would also like to thank my academic peers in the acoustics program at UT, especially Robert Taylor and Abdelaziz Rhazzali, for their friendship, support, and late night study-discussions. I'd like to acknowledge the members of the UT Student Veterans Association for their actions in supporting student veterans. Finally, I'd like to thank my family for enabling me to take risks and follow my dreams. This work was supported by the Office of Naval Research.

Marine Sediment Characterization Through Echo Sounder Measurement Analysis

Lucas Ryan Shearer, M.S.E.
The University of Texas at Austin, 2020

Supervisor: Mark F. Hamilton
Co-Supervisor: Aaron M. Gunderson

Echo sounder measurements were used to quantify bottom loss from muddy seafloors during the Seabed Characterization Experiment (SBCE), and at the Dauphin Island Sea Lab (DISL) in 2017. Data were processed with a combination of matched and bandpass filters to obtain metrics which describe the magnitude and shape of the bottom reflection return. While the SBCE measurements were gathered at normal incidence, many of the DISL measurements were taken at significantly larger incident angles. Those data collected at near-normal incidence were used to estimate geophysical properties through the application of existing empirical regression equations. Data collected at oblique incidence were used to determine sediment sound speed and density ratios through a two-parameter inversion, using the flat interface Rayleigh reflection formula. The estimated values were compared to *in situ* and laboratory ground truth measurements. The accuracy of each approach and the causes

of bottom loss variability (bioturbation, gradients, inhomogeneities, etc.) are discussed.

Table of Contents

List of Tables

List of Figures

Chapter 1

Introduction

Beyond traditional water depth measurements and fish finding applications, echo sounding has enabled the study of the seafloor and its geophysical properties.[1] Acoustic waves are a useful mechanism for observing the seafloor because they propagate through the water column with little attenuation and offer a measurable reflection. The magnitude and phase of the reflected acoustic signal generally depends upon the characteristic impedance of the sediment as well as the interface roughness, sediment volume properties, and sediment layering. Measurements can be made remotely and autonomously, facilitating the survey of large swaths of seafloor quickly and non-invasively.[2]

As an acoustic waveform propagates, it becomes altered by the environment with which it interacts. The waveform, specifically one which has reflected off of the ocean sediment, becomes imprinted with information related to the geophysical properties and environmental attributes of the seafloor (sediment type, density, porosity, grain size distribution, wave speed, attenuation, tortuosity, bathymetry, layering, surface roughness, etc.);[3] the process of estimating those sediment properties from acoustic echos is referred to as acoustic sediment characterization or classification. Many challenges are en-

countered during acoustic sediment characterization because the ocean is a complex and dynamic environment with interdependencies that may not be fully understood, e.g. biological effects, ocean currents, sediment layering, clutter, etc.

1.1 A Brief History

Before the invention of modern electronics, sailors measured water column depth and surficial sediment composition using a technique known as lead and line sounding. The term *sounding* derives its meaning from the languages of Old and Middle French, *sonde* ("sounding line") and *sonder* ("to plumb"). Soundings were conducted by lowering a plummet, traditionally made of lead, to the seafloor. The lead weight was tied to a line of rope with depth markings so that the crew leadsman could readily measure and report depth findings. This method of lead and line sounding was unreliable in deep water, a long rope was heavy and would continue to fall under its own weight even after the lead had reached the bottom. And if the ship was traveling, the translation of the ship would cause the rope to fall at an angle.

Commonly, the lead was coated with grease or tallow. Ocean sediment would stick to the tacky coating and be collected for review and cataloging, helping the ship's pilot to recognize location and navigate safely. The device had a difficult time collecting heavy particles like pebbles and boulders because they would become unstuck from the tool while surfacing. This led scientists of the day to reason that ocean floors were comprised mostly of fine

particles: sand, silt, and clay.[4,5] Future iterations of the lead included scoops or substrate penetrating pipes.

Mechanical sounding machines were developed to measure features of the deep-ocean, in part to assist with the installation of a transatlantic communications cable. One significant improvement of the sounding machine is attributed to Sir William Thomson (Lord Kelvin) when he successfully used piano wire as the sounding line. The wireline sounding machine would stay relevant for many decades and resulted in the first modern bathymetric maps.[5]

Sounding technology significantly advanced in the face of tragedy, specifically after the sinking of the RMS Titanic and during the First World War. The development of underwater acoustic technology became focused on horizontal propagation for the detection of icebergs and submarines.[6] During one of these experiments a Canadian-American inventor by the name of Reginald Fessenden, along with his co-workers, successfully identified underwater acoustic signals reflected by a distant iceberg using a loudspeaker-like transducer invented by Mr. Fessenden and bearing his name, the Fessenden Oscillator. A much nearer echo was also detected and subsequently attributed to the ocean bottom, demonstrating that soundings could be taken using methods other than weighted line.[5] This resulted in a patented method and apparatus for determining distance by echo. The same effort was being made at the same time by a German physicist, Alexander Behm, who secured a German patent for an echo sounder a few years before Fessenden, however he did not market the device until the 1920s.[7] Soon after, the piezoelectric transducer became a

viable tool and has since become the most common electromechanical transducer used for SOund Navigation And Ranging (SONAR).

1.2 Motivation for Remote Sediment Characterization

Sediment sample collection methods have benefited from technological advancement since the days of the tallow coated lead weight. Examples of modern technology include human divers, underwater video, and remotely operated vehicles. Still, the most common sampling methods, e.g. surficial grab and penetrating cores, are often inadequate.

Laboratory measurement techniques have also continued to develop at a rapid pace. Electron scanning microscopy produces highly magnified images for observing sediment grains[8] while acoustic core logging systems measure depth dependent sound speed and attenuation.[1,9,10] The resulting measurements provide invaluable and necessary ground truth evidence of the physical and geoacoustic properties of ocean sediment. For more information about common sampling and analysis practices, the reader is pointed to a document published by the Army Corps of Engineers detailing procedures for handling sediment and water samples [11].

Unfortunately, sample collection and the subsequent laboratory analysis is expensive, time consuming, and only representative of one point location at one moment in time.[12–14] Further, sediment collection is an intrusive operation which may disturb the sediment sample and alter bulk properties during collection, transport, and analysis. Thus, observing the undisturbed sediment

in situ is preferred albeit requires a different approach. One of those approaches is an *in situ* acoustic measurement system where probe transducers are placed in the sediment and acoustic propagation through the sediment is measured.[15,16]

Another approach, and the subject of this study, is an active sonar system with which acoustic signals are reflected from of the water/sediment interface and the loss is quantified and related to geophysical properties of the sediment. Acoustic interactions at the sediment interface are complex and there is no simple relationship between the acoustic backscatter and the sediment type and structure.[17] That said, it has been shown that acoustic backscatter can be used to classify the seafloor.[13,18–20]

Acoustic seabed characterizations can provide important and functional information to industrial, scientific, and military entities.[17,21,22] Civil coastal infrastructure and off-shore resource development relies on surficial sediment and sub-bottom layering data to inform the placement of pipelines, cables, pilings, footings, moorings, anchors, etc.[22] Benthic ecologists use habitat classifications and seabed characteristics in the study of organisms which live in and on the seafloor while also assessing the health of those bottom-dwelling ecosystems.[23]

1.3 Organization

This thesis studies acoustic backscatter data gathered by remote sensing during two field experiments and applies empirical regressions to infer sed-

iment properties. A method for processing single beam sonar data is presented along with physics-based metrics and empirical regression equations that are used to estimate physical and geoacoustic properties pertinent for engineering application and scientific observation. Those metrics and derived/empirical properties are compared to ground truth measurements where available.

Chapter 2 provides background information on the signal processing topics and methods used to detect and measure the amplitude of a signal of interest buried in white Gaussian noise. Chapter 3 presents an analytical solution for the acoustic reflection coefficient, introducing metrics by which geoacoustic properties can be estimated. Chapter 4 describes the hardware used to collect acoustic reflection data and the signal processing methods used to obtain bottom loss measurements. The field experiments are introduced along with background information, processed data, and results. Ground truth comparison is used to validate these results. Chapter 5 provides a review and concluding remarks.

Chapter 2

Signal Processing

2.1 Discrete Time Signals and Aliasing

The following is a review of the signal processing necessary for acoustic sediment classification. When a dynamic pressure sensor, such as a hydrophone, is exposed to an acoustic pressure field, it will ideally output a voltage signal proportional to the sensed pressure. The voltage signal must then be routed through an analog anti-alias filter. This filter attenuates high frequency components of the analog signal to satisfy the Nyquist-Shannon sampling theorem; the theorem is reviewed in this section. A data acquisition system converts the low-pass filtered analog voltage signal into a digital format to be recorded and stored. The digital samples represent instantaneous pressure values at specific moments in time, governed by the sampling rate of the digital data acquisition system and the sensitivity of the transducer.

Periodic sampling can be expressed mathematically through the use of a Kronecker delta function.[24,25] Here, $x(t)$ represents a continuous analog signal, and $x_s(t)$ the periodically sampled version.

The sampled signal can be expressed as

$$x_s(t) = \sum_{n=-\infty}^{\infty} x(nT_s)\delta(t - nT_s). \tag{2.1}$$

The impulse train is periodic with T_s, the inverse of the sample rate (F_s), and can be expressed using a discrete Fourier series as a sum of complex exponentials. By a Fourier transform, and application of the shifting property, the spectral content of the sampled signal can be shown to be

$$X_s(f) = \frac{1}{T_s} \sum_{n=-\infty}^{\infty} X(f - nF_s). \tag{2.2}$$

This result indicates that the double-sided frequency spectrum of the sampled signal is proportional to that of the continuous signal provided that two conditions are met.

1. A band-limited continuous spectrum, $-f_{\max} \leq 0 \leq f_{\max}$. These bounds explicitly show the double-sided nature of the frequency spectrum, positive and negative. The concept of negative frequencies is essential when using complex numbers to describe sinusoidal waves. The evidence for this is found in Euler's formula which can be written to show that $\sin(\omega t) = \frac{e^{j\omega t} - e^{-j\omega t}}{2j}$. The sign of an angular frequency can be illustrated as the direction of phasor rotation in complex space.

2. The sampling frequency, F_s, is sufficiently large such that replicate spectra, where $n \neq 0$, do not interfere with the original where $n = 0$. Therefore, the sampling frequency should be chosen to be at least twice that of the upper band-limit of the signal.[25,26] This proof and result is known as the Nyquist-Shannon sampling theorem and the Nyquist cutoff frequency:

$$f_{\text{Nyquist}} = \frac{F_s}{2}. \tag{2.3}$$

The motivation behind Nyquist-Shannon sampling theory is that one would like to exactly reconstruct the original time history, $x(t)$, from the discretized time series, $x_s(t)$. It is possible to do this if the frequency spectrum of the time series, $X_s(f)$, is not overlapped or indistinguishable from the spectral replications, and presuming $x(t)$ is periodic in time. In practice, the reconstruction can be a very good approximation depending on how many Fourier coefficients one wishes to calculate.

As a visual example, Figure 2.1 displays how an undersampled time history can cause ambiguities in the frequency content of the signal. This is called aliasing. The black line represents a real 7 Hz signal and the red circles represent sampled locations with a sample rate of 5 Hz. With this sample rate, it is impossible to determine whether the measured time series represents a 2 Hz signal or a 7 Hz signal. By sampling at a proper rate, the digitized data is unambiguous in its spectral content. The Nyquist-Shannon sampling theorem shows that a signal should be sampled at a rate which is at least two times the highest frequency of interest, in this example that rate is 14 Hz.

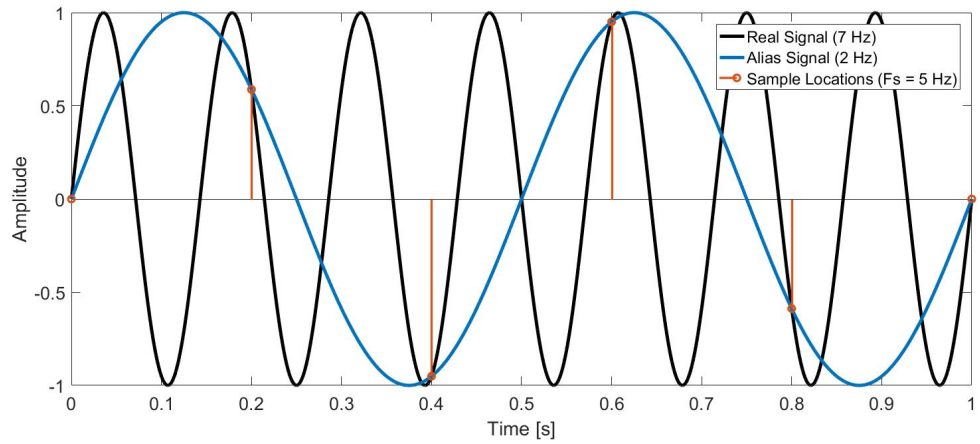

Figure 2.1: Aliasing example of an undersampled waveform

Aliasing is one of many issues which can occur during testing, especially if that test is conducted without proper preparation. If the time history is ambiguous in frequency content there is no way to correct it,[25] so it is important to conduct time domain and frequency domain checks in order to validate the data recording setup. Those checks can include a visual inspection of the time histories with special care taken to observe signal drift, data dropouts, clipping or digitization errors, etc. Frequency domain checks can include calculating the power spectral density of a received signal and verifying the sampling is sufficient and all energy is captured, a Parseval's theorem check. It is also useful to measure background noise levels before and after testing, or at any time that changes are made to the test configuration. For underwater testing, this includes understanding how the data acquisition setup responds to changes in depth and the resulting changes in ambient hydrostatic pressure as this can affect the sensitivity of the hydrophone.

2.2 Matched Filter

A matched filter is the optimal constant linear filter for maximizing the instantaneous signal-to-noise ratio (SNR) at the moment when a signal of interest is received.[26–29] The proof of the matched filter is well documented, especially as it relates to radar. It is shown in [26–29], and summarized in this section, that the optimal filter's impulse response and frequency response functions are the time-reverse and complex conjugate of the real signal of interest, respectively. Every unique signal of interest has its own optimal filter whose impulse response and frequency response is matched to its waveform shape and spectral content, hence the name "matched" filter. Therefore, when designing a matched filter it is necessary to know *a priori* the waveform of interest and an estimated noise type. This section summarizes and highlights key aspects of the filter as documented in [26–29].

The purpose of the matched filter is to maximize the instantaneous SNR of its output at a decision time, t_d, when a signal of interest is present. The decision time is defined as the moment when the entirety of that signal has been received. This corresponds to the time shift in the linear time-invariant filter's convolution process when the received signal of interest and the filter impulse response become exactly overlaid, resulting in a maximization of the filter output. This is especially useful when identifying signal arrival times and amplitudes in noisy environments.

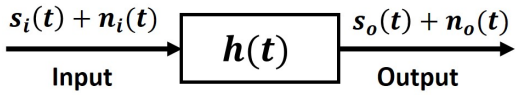

Figure 2.2: Linear time-invariant (LTI) filter. The left hand input to the LTI represents a recorded time series data set. The right hand side represents the matched filter output. The output is equal to the convolution of the input, $s_i(t)$, and the filter's impulse response, $h(t)$.

The instantaneous SNR is defined here as the ratio of output signal and noise powers,

$$\mathrm{SNR}(t) = \frac{|s_o(t)|^2}{|n_o(t)|^2}. \tag{2.4}$$

Figure 2.2 illustrates the linear time-invariant filter which convolves the input signal, $s_i(t)$, with its impulse response, $h(t)$. The numerator in Eq. (2.4) is the square of the matched filter output. It can be shown by the convolution theorem to be equal to the inverse Fourier transform of the frequency domain product,

$$s_o(t) = h(t) * s_i(t) = \int_{-\infty}^{\infty} H(f) S_i(f) e^{j2\pi ft} df. \tag{2.5}$$

The instantaneous signal power at decision time t_d is thus,

$$|s_o(t_d)|^2 = \left| \int_{-\infty}^{\infty} H(f) S_i(f) e^{j2\pi f t_d} df \right|^2. \tag{2.6}$$

The noise terms can be treated in a similar manner as the signal,

$$n_o(t) = h(t) * n_i(t) = \int_{-\infty}^{\infty} H(f) N_i(f) e^{j2\pi ft} df. \tag{2.7}$$

The analysis below follows the simple case of additive white Gaussian noise (AWGN). However, the general noise spectrum term, $N_i(f)$, can represent all

colors and distributions of noise.[26] White Gaussian noise has a constant power spectrum, indicating that all frequencies are present and equally weighted with a Gaussian amplitude distribution at each frequency. The total power of the noise is equal to the product of its constant power spectral density, η, and the total bandwidth, B. The total power in the two-sided power spectrum is[a]

$$P(f) = \int_{\frac{-B}{2}}^{\frac{B}{2}} |N_i(f)e^{j2\pi ft}|^2 df = \eta B, \tag{2.8}$$

and the noise power in the matched filter output is

$$|n_0|^2 = \int_{-\infty}^{\infty} |H(f)N_i(f)e^{j2\pi ft}|^2 df \tag{2.9}$$

$$= \eta \int_{-\infty}^{\infty} |H(f)|^2 df. \tag{2.10}$$

Finally, the entire ratio for the white noise case is written as

$$\mathrm{SNR}(t_d) = \frac{\left| \int_{-\infty}^{\infty} H(f)S_i(f)e^{j2\pi ft_d} df \right|^2}{\eta \int_{-\infty}^{\infty} |H(f)|^2 df}. \tag{2.11}$$

The Cauchy-Bouniakowsky-Schwarz inequality[30] is used to determine the optimal transfer function, $H(f)$, which maximizes the output SNR. The inequality is an integral representation of the Cauchy-Schwarz inequality and shows that the inner product of two functions becomes maximized when one is a scaled version of the complex conjugate of the other. This is analogous to the maximum dot product of two vectors in real space occurring when those

[a]Note that the two sided bandwidth is equal to B. Different definitions of the total bandwidth ($2B$) and constant power value ($\eta/2$) may result in a coefficient of two in the final formulation of SNR, as seen in [26].

two vectors are oriented in the same direction. The resulting expression for the optimal filter's frequency response function which maximizes the SNR in the presence of AWGN is shown by equation 7.16 in [26] and recited here,

$$H(f) = S_i^*(f)e^{-j2\pi f t_d}. \tag{2.12}$$

Finally, by taking the inverse Fourier transform of Eq. (2.12) and applying the shifting theorem, the optimum impulse response of the matched filter is written as

$$h(t) = s_i^*(t_d - t). \tag{2.13}$$

This result proves that the optimal filter impulse response which maximizes the SNR of a real signal of interest combined with AWGN is the time-reverse of the original.[b] An example of the matched filter is provided in [25] on pages 378 - 379.

2.3 Pulse Compression and Side Lobe Supression

Limitations of active sonar systems include range resolution and SNR, and contradictory solutions exist to address each.[26,29] An increase in range resolution can be attained by using very short duration output signals. This reduces the chance of overlapped returns from closely spaced reflectors, allowing finer spatial resolution. The trade-off is a decrease in SNR because short duration output signals have reduced time average transmitted power compared

[b]The complex conjugate of a real signal is the signal itself. The conjugate notation in Eq. (2.13) is kept for completeness.

to a signal with the same amplitude but a longer duration.[26,29] The benefits of high SNR and increased range resolution are realized through the use of signals whose carrier frequency is modulated in time. A receiving filter that exploits this relationship between time and frequency allows the output signal's duration to be increased without sacrificing range resolution. It is shown in this section that a linear frequency-modulated (LFM) signal achieves an increase in range resolution without decreasing SNR. The process is known as pulse compression. The LFM signal is referred to in this section as a sine-sweep or a chirp.

It is beneficial for the purposes of signal detection to choose a signal of interest, and thus define its replica matched filter template, which will provide a sharp and discernible pulse in the matched filter output. Pulse compression increases the likelihood of correctly identifying a signal arrival and finely resolving that arrival in time. As an example, three common signal shapes are considered: rectangular, sine, and sine sweep. In Figure 2.3 the three signal shapes are shown to produce different output pulse shapes. In each case the "input" contains two signals of interest, one of unity magnitude and another whose magnitude is halved. The signals of interest are summed with AWGN of root-mean-square amplitude 20% relative to the unity signal's maximum amplitude. The reason for including two signals of interest is to demonstrate that the magnitude of the pulse in the matched filter output is nearly proportional to its respective input signal's amplitude. In ideal conditions, or after coherent averaging, the output pulse peak value is proportional to the input

signal's amplitude.

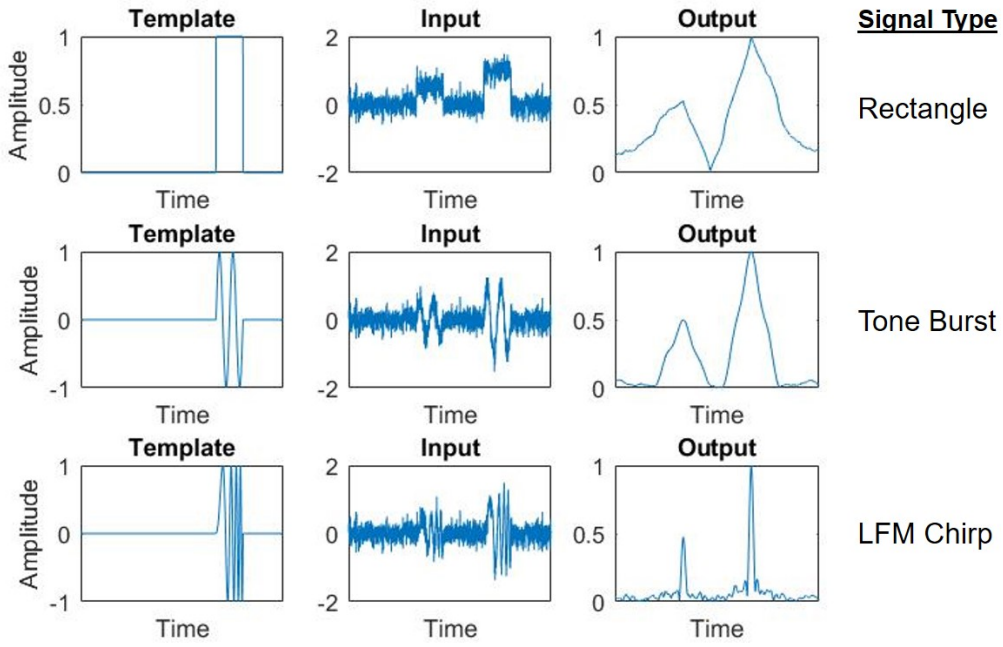

Figure 2.3: Comparing replica template signals (left) and their respective matched filter outputs (right). The input signal (center) includes two signals of interest with 20% relative root-mean-square amplitude AWGN. Each plot has the same horizontal window, representing time.

As a comparison, Figure 2.4 represents the same scenario but with a reduced SNR. The root-mean-square amplitude of the AWGN is set to 100% relative to the unity signal's maximum amplitude.

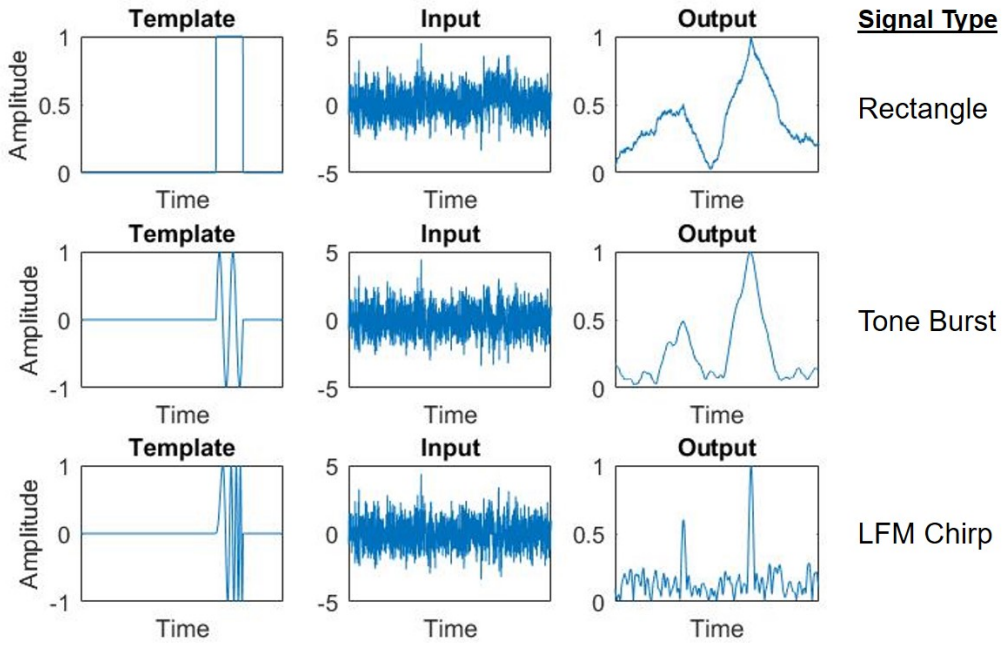

Figure 2.4: Comparing replica template signals (left) and their respective matched filter outputs (right). The input signal (center) includes two signals of interest with 100% relative root-mean-square amplitude AWGN. Each plot has the same horizontal window, representing time.

In this demonstration, it is noticeable that the output for the rectangular and sinusoidal waveform cases are more ambiguous in identifying the arrival times of the signals of interest, increasingly so as the input SNR is lessened. In contrast, the sharp compressed pulses resulting from use of the sine-sweep more clearly resolve the moments of arrival. A pulse compression filter takes advantage of the time delay vs. frequency characteristic of the chirp, producing a narrow pulse in the filter output.[29] The magnitude and width of the compressed pulse envelope can be determined by following the

analysis contained in [27, 29, 31] and is shown to depend upon the bandwidth and duration of the waveform of the signal of interest.

A mathematical representation of an LFM chirp is written as,

$$s_i(t) = \begin{cases} \cos\left(2\pi f_0 t + \dfrac{2\pi\Delta f t^2}{2T}\right) & |t| \leq \dfrac{T}{2} \\ \\ 0 & |t| > \dfrac{T}{2} \end{cases} \tag{2.14}$$

The signal is non-zero over the time interval $\frac{-T}{2} \leq t \leq \frac{T}{2}$, thus defining the LFM signal's duration as T. The modulation in frequency is centered at f_0, ranging the instantaneous frequency from $f_0 - \frac{\Delta f}{2}$ to $f_0 + \frac{\Delta f}{2}$. The total change in instantaneous frequency is defined as the bandwidth of the signal, $B = \Delta f$.

In [27, 29, 31], a simplification is made by considering only the positive component of the frequency spectrum of Eq. (2.14). To follow along with this non-symmetry in the frequency domain and to implement this simplification in an experimental data processing method, a bandpass filter is applied. The filter is designed to remove the negative frequency component. This can be done mathematically by expressing s_i as a sum of complex exponentials via Euler's formula and eliminating the negative frequency component. The result is a conveniently written complex signal of positive orientation and remains bound by $|t| \leq \frac{T}{2}$. Written with a normalized amplitude and explicitly including a rectangular shading function yields,

$$s_i(t) = \text{rect}\left(\frac{t}{T}\right) e^{j2\pi(f_0 t + \frac{Bt^2}{2T})}. \tag{2.15}$$

The rectangular function[c] envelopes the signal and is equal to unity over the interval $\frac{-T}{2} \geq t \geq \frac{T}{2}$ and zero when $|t| > \frac{T}{2}$. The spectrum of the matched filter was shown in Eq. (2.12) and is rewritten using the filtered signal from Eq. (2.15),

$$H(f) = S^*(f)e^{-j2\pi ft} = \int_{-T/2}^{T/2} e^{j2\pi[(f-f_0)t-\frac{Bt^2}{2T}]}dt. \tag{2.16}$$

The evaluation of this integral is well documented.[27,29,31] The spectrum of the optimal filter is provided as Eq. (14) in [27] and Eq. (18) in [31] as

$$H(f) = e^{j\pi\frac{T}{B}(f-f_0)^2}. \tag{2.17}$$

Equation (2.5) can be written in terms of the convolution integral, evaluated, and reorganized.[27,32] The output of the matched filter becomes,

$$s_0(t) = \sqrt{TB}\,\mathrm{sinc}(Bt)e^{j2\pi(f_0t-\frac{Bt^2}{2T})+\frac{j\pi}{4}}. \tag{2.18}$$

The normalized sinc function is used here, $\mathrm{sinc}(x) = \frac{\sin(\pi x)}{\pi x}$.

Of importance to this discussion of pulse compression is the magnitude of the matched filter output, $|s_0(t)| = |\sqrt{TB}\,\mathrm{sinc}(Bt)|$. The peak amplitude of a matched filter output is proportional to $\sqrt{TB}$. The argument inside of the square root is commonly known as the time-bandwidth product. Thus, the maximum SNR can be boosted by increasing the time-bandwidth product. The shape of the compressed pulse is defined by a sinc function. The total null-to-null width of each side lobe, and the half-width of the main lobe near the

[c]The rect function has a few alternative definitions for values at the endpoints (0, 1/2, or undefined). For ease of analysis the value of 1 is used.

-4 dB point, is proportional to the inverse bandwidth, $\frac{1}{B}$. The sinc function has significant first side lobes, nearly -13 dB compared to the main lobe. Side lobes can cause false positive signal identifications and are one of the drawbacks of pulse compression.

Chapter 3

Acoustic Reflection and Sediment Characterization

3.1 Overview

This chapter begins by describing common geoacoustic models, more complete detail of which is found in [33]. The motivation for Section 3.2 is to identify advantages and disadvantages of different model types for use in sediment characterization. A common aphorism goes like this, "All models are wrong, but some are useful".[34] We seek to use the least complicated model available which accomplishes our goal of sediment characterization by near-normal incidence echo sounding.

Section 3.3 reviews the analytical solution of acoustic reflection from a flat interface. The simplest case assumes an ideal two fluid medium. The term "reflection" is used to describe the process instead of the more general term "scattering" and refers to the return from a flat, partially reflecting, interface in the specular direction.[33] The system setup and simplifying assumptions seek to mimic field experiments considered in Chapter 4.

In 2019, Isakson et al.[2] reviewed statistically and physically derived metrics for quantifying seafloor bottom reflection. It was determined that the

physically derived metrics based on features of the compressed pulses were more robust than the statistical metrics in a model/data comparison study. The physically derived metrics will be defined and discussed in Section 3.4.

In this document, the term "geophysical properties" encompasses both the physical properties (i.e. mean grain size, porosity, permeability, bulk density, grain and pore characteristics, and sediment type) and geoacoustic properties (i.e. wave speed, attenuation, bulk density, and specific acoustic impedance) of a sediment.[33] Bulk density is purposely referred to as both a physical and geoacoustic property. The calculation of geophysical properties will be discussed in Section 3.5.

3.2 Sediment Representation and Geoacoustic Models

Physical and geoacoustic properties are related through complex interdependencies, the physics of which are modeled using different types of media including fluid, elastic, and poroelastic.[33,35] These media, and the models which utilize them, range in scope and complexity. Chapter 2 in [33] introduces how these media are used to represent marine sediments. Figure 2.4 in [35] summarizes key aspects of geoacoustic models including the requisite number of input parameters, medium type, model type, and loss mechanisms.

Although marine sediments are comprised of discrete particles, sediments are commonly approximated as continuous media when acoustic wavelengths are much larger than the size of any one particle.[33] Continuum mechanics describes physical material properties as a bulk average of the effective

medium. Very high frequency scattering from individual grain particles are not of concern in this study.

Some types of sediment are well approximated by the simplest of media, fluid. Sediment with small unconsolidated grains (silt/clay) and high water content are often approximated as a fluid in which only compressional waves are supported. The acoustic stresses in the sediment can be described appropriately by a pressure field and accompanying wave equation.[33] Loss mechanisms may be accounted for through the use of a complex wave number in the model wave equation. There are three input parameters for a simple fluid model including attenuation in the sediment, sound speed ratio and bulk density ratio of the sediment and sea water.

While the fluid model addresses the compressional wave aspects of the problem, many sediments support significant compressional and shear modes. Therefore, an elastic-solid representation may be desirable. Sediments with fast shear wave speeds, as found in a consolidated rocky seafloors, cause significant discrepancy between reflection coefficients calculated by fluid and elastic models, see Figure 9.4 in [33]. Isotropic elastic models require five input parameters, three of which are the same as in a fluid model. The introduction of shear waves requires two new parameters, shear wave speed and shear wave attenuation.

Poroelastic representation introduces significant complexity by treating the sediment as a two-phase medium. The sediment grains are considered to make up a porous consolidated elastic skeleton whose pores are filled with

fluid.[36–38] Poromechanics allows for relative motion between the frame and fluid constituents of the medium. Development of the poroelastic model is attributed to Maurice A. Biot and was reparameterized for ocean sediment acoustics by Robert D. Stoll. The derived geoacoustic model type bears their names, the Biot-Stoll model.[36–39] Biot theory requires a minimum of thirteen parameters,[33] many of which are not measurable and are often determined by inverse methods. A number of improvements to the Biot-Stoll model have been developed, seeking to increase accuracy or usability by either accounting for more complex physical mechanics[39] or by consolidating poroelastic effects into an effective density for use in the simple fluid model.[40]

Elastic and poroelastic models are significant refinements of fluid models when shear wave speeds in a marine sediment are non-negligible. However, the application of these models, and the methods required to obtain estimates of sediment properties, can be cumbersome. Ground truth validation of many model parameters may not be possible (frame moduli, frame log decrement, pore size parameter, strain hardening index, compressional rigidity coefficient, shear rigidity coefficient, shear and compressional viscoelastic relaxation time).

Often the measured wave speeds and attenuation are the only model-data comparison.[35] The compressional wave remains the most important mechanism in unconsolidated fine grain sediment, the physics of which can be simply modeled using fluid theory. Recognizing that there is a trade off between accessibility and accuracy, the reflection coefficient and impedance relations derived with ideal fluid approximations are used in this study. A

combination of empirical regression and a simple parameter inversion are used to infer geophysical properties.

3.3 Acoustic Reflection from a Fluid-Fluid Interface

Consider an acoustic point source that emits a waveform which propagates through a lossless fluid medium with density ρ and sound speed c. The specific acoustic impedance for an outgoing spherical wave can be found using a solution of a forward propagating wave which satisfies the linearized lossless wave equation.[41,42] The acoustic pressure is written as p and described by amplitude A, traveled distance r, wavenumber k, and angular frequency ω,

$$p(r,t) = \frac{A}{r} e^{j(\omega t - kr)}. \tag{3.1}$$

The relationship between acoustic pressure and radial acoustic particle velocity, u_r, for a one-dimensional spherically diverging wave can be found using the linearized Euler momentum equation as shown in [42], pp. 359-361,

$$\rho \frac{\partial u_r}{\partial t} = -\frac{\partial p}{\partial r}, \tag{3.2}$$

$$u_r(r,t) = \frac{A}{\omega\rho}\left(\frac{k e^{j(\omega t - kr)}}{r} - \frac{j e^{j(\omega t - kr)}}{r^2}\right). \tag{3.3}$$

The specific acoustic impedance is defined as the ratio of acoustic pressure to acoustic particle velocity. Written in terms of an outgoing spherical wave,

$$Z_{sphere} = \left(\frac{p}{u_r}\right)_{outgoing} = \rho c \left[\frac{1}{1 + \frac{1}{jkr}}\right]. \tag{3.4}$$

If $kr \gg 1$, the specific acoustic impedance of an outgoing, time-harmonic, spherical wave approaches the characteristic impedance of the medium,[41,42] $Z = \rho c$. The characteristic impedance of a medium is the specific acoustic impedance of a plane wave in free space. A spherically diverging wavefront can be described as locally planar when the radius of curvature is sufficiently large. If the acoustic wave is incident on a flat[a] interface between two fluids, each with their own characteristic impedances, the wave will become reflected, transmitted, or some combination of the two.

The reflection and transmission of obliquely incident plane waves is well addressed in many fundamental and introductory texts.[41–43] The Rayleigh reflection coefficient is expressed as a function of the characteristic impedances of each fluid halfspace and the angles of incidence and transmission,[41]

$$R = \frac{Z_2 \cos(\theta_i) - Z_1 \cos(\theta_t)}{Z_2 \cos(\theta_i) + Z_1 \cos(\theta_t)}. \tag{3.5}$$

The expression becomes simplified if the acoustic wave is incident at a near-normal angle where $\cos(\theta) \approx 1$. At normal incidence, the unknown input impedance of the underlying medium, Z_2, can be fully determined if R and Z_1 are known. This analytical solution of plane waves obliquely incident on a flat interface can be extended to include multi-layered media environments.[44] If the discretized layers are thin and each layer's properties are similar to their

[a]The interface between two fluids does not remain flat as it is exposed to oblique angle incident pressure wave. Acoustical disturbance causes the interface to flex and oscillate. If the angle of incidence is small and the trace velocity is supersonic with respect to the second medium, $\sin(\theta) < c_1/c_2$, the disturbance propagates into that medium as a plane wave.[43]

neighbors, a pseudo-gradient can be modeled. Layered sediments affect the input impedance at the sediment/water interface, complicating the inference of geophysical properties from experimental data. For sediments with sufficiently thick layers the input and characteristic impedances are assumed equal. In this case, it is hypothesized that the experimentally measured reflection coefficient provides a means to infer the geoacoustic properties of a sediment.[20]

A portion of Chapter 4 will utilize the angular dependence of $R(\theta)$ because of the geometry of the experimental test setup. Data collected during the Dauphin Island Sea Lab Experiment (DISL) is not assumed to be collected at normal-incidence. Therefore, the characteristic impedance of the sediment cannot be fully-determined as the transmitted angle was not measurable with the test setup used in the DISL experiment.

3.4 Bottom Loss, FWHM, and HWHM Ratio

Echo sounding, as described in Chapter 1, measures the two-way travel time of an acoustic wave between a source/receiver position and the seafloor. To do this, some measurable amount of the source acoustic energy must reflect from the water/sediment interface and return to the receiver location. The return signal will be of diminished amplitude for two main reasons, presuming a flat seafloor. The first is due to geometrical spreading and the second is due to partial transmission of energy into the seafloor.

In experimental measurement, many loss mechanisms are inseparable from coherent reflection loss (e.g. roughness and volume scattering, layer-

ing, gradients, entrained gas in the sediment or water column, and near-field effects).[33] These mechanisms cause discrepancies between experimental and model-based estimates of geophysical properties. Bottom loss is reported in decibels,

$$BL = -20 \log_{10} \frac{\text{Pressure Signal Received}}{\text{Pressure Signal Transmitted}}. \tag{3.6}$$

Bottom loss is of significant interest to this study as a means of direct observation of the sediment/acoustic interaction. From this observation, the inference of geophysical properties is achievable.[20] Bottom loss can be measured experimentally as the difference between the reference and reflected compressed pulse peak heights in the spreading loss corrected output of a matched filter. Section 4.2 discusses the experimental setup which enables the recording of a direct path reference signal and a bottom reflected signal.

In an ideal environment, the spreading correction is the only necessary action taken to recoup the amplitude of the reflected signal. In reality, reflection measurements are affected by loss mechanisms which are unaccounted for in a lossless flat interface fluid model. This may cause an underestimation of the magnitude of the reflection coefficient, and therefore an underestimation of sound speed and density. Detail on the difficulties of reflection measurement can be found in Chapter 11 of [33].

Besides peak height, there are two other compressed pulse characteristics of interest, the full width at half max (FWHM) and the ratio of half width at half max (HWHM). The FWHM is a measure of the pulse width at its half power point (-3 dB). Summarized in Chapter 2 was the fact that the width of

a compressed pulse depends on the bandwidth of the LFM chirp. From [2], the theoretical FWHM of the compressed pulse is $0.886/B$. The FWHM of experimental data will be wider than the ideal limit due to a nonuniform spectral response in the measurement system. Additionally, a number of environmental factors contribute to a widening of the FWHM. These include interface scattering mechanisms, volume scattering in the sediment, and density/sound speed fluctuations.

The ratio of HWHM is a measure of skewness of the compressed pulse, calculated by dividing the width of the early half of the pulse by the width of the late half of the pulse. It can depend on the frequency response of the measurement system as well as environmental factors. Such skewness may result from spreading loss, reverberation, scattering, dispersion, frequency dependent attenuation, and others. In numerical simulation trials, the ratio of HWHM has shown to be the least sensitive of the three metrics.[2]

The coefficient of variation (CV) is a dimensionless metric used for quantifying deviation, defined as the standard deviation divided by the mean. It is useful when comparing the fluctuation of parameters such as BL, FWHM, and ratio of HWHM. It enables a comparison both between parameters and between experiments. For example, the FWHM for two different experiments using two different bandwidths would be very different. However, the fluctuation of FWHM could be compared using CV.

3.5 Geophysical Properties and Empirical Regression Equations

Relationships between physical and geoacoustic properties of marine sediments have been studied for decades, pioneered in part by scientists and engineers such as Hamilton,[45] Shumway,[46] Nafe,[47] Nolle,[48] Wood,[49] Hampton,[50] Mackenzies,[51] Brekhovskikh,[44] Urick,[52] and many others. From those early studies, it became widely accepted that acoustic observations made in the ocean could be well predicted by acoustic models of layered fluid-like sediments by using laboratory-measured values of density and sound speed. Modern sediment characterization uses acoustic measurements to predict physical properties, relying less on expensive laboratory ground truth measurements.[12,13,21,22] Future predictive technology may still require some tuning through ground truth.[53]

Both physics-based and empirical models have been used to relate physical and geoacoustic properties. Empirical relationships are often used to validate the analytical sediment representations. Complex physics-based models like Biot-Stoll have input parameters which are difficult to measure. This limits their predictive capacity in unfamiliar environments. Other physics-based models[54] have used empirical relationships to derive unknown constants. Empirical relations between physical and geoacoustic properties have many advantages in both sediment characterization and in validation of physical models. For these reasons, it is a useful tool for this experiment.[33]

The definitions of a physical and geoacoustic property vary depend-

ing on reference text or working group. Some properties may be attributed to both categories, such as bulk density. The definitions in this document are founded in the text of Jackson and Richardson, [33]. The physical properties of significant interest to this study include mean grain size, porosity, and bulk density. The geoacoustic properties of interest are the density ratio, sound speed ratio, and volume attenuation. Interface roughness can also affect experimental bottom loss measurements, but is not considered a geophysical property. Roughness and layer thickness are better categorized as environmental parameters rather than intrinsic properties.

3.5.1 Core Data and Index of Impedance Regressions

To relate physical and geoacoustic properties of marine sediment Jackson and Richardson in [33] published a set of empirical relationships.[33,55] The parameters reported include sediment sound speed, sediment sound speed ratio, attenuation, mean grain size, sediment porosity, sediment bulk density, index of impedance, and sediment type.

The index of impedance, IOI, is introduced to decouple the sediment's characteristic impedance from seasonal variations in the temperature and salinity of pore water in the sediment.[33,55] The IOI is the product of sediment bulk density and the sound speed ratio and has been used with good success to estimate values of sound speed ratio, bulk density, and porosity.

$$IOI = \frac{\rho_2 c_2}{c_1} \tag{3.7}$$

The index of impedance regression equations are based on thousands of measurements from more than 124 cores collected from over 65 different geographical sites, shown in Figures 5.12 and 5.13 in [33]. The method for handling the core samples and measuring these properties are described in [55]. A 400 kHz pulsed sine wave was transmitted from one wall of the coring tube to the other. The signal's time of flight and amplitude attenuation were compared to the same experiment conducted with core tubes filled with a well characterized substance, distilled water. After the acoustic experiment for each core was concluded, the sediment was dried to determine porosity and the grain density was measured. The bulk density was calculated using measured values of the pore water and grain densities and the porosity of the sediment. Grain sizes were determined using a number of techniques either by sieve, pipette, or sedigraph.[55]

IOI regression equations can be used to estimate values of physical properties including bulk density (ρ [g/cm^3]), porosity (η [%]), and mean grain size (M_z [ϕ])[b], and geoacoustic properties including the sound speed ratio (SSR [m/s]), and acoustic attenuation coefficient (k [dB/m/kHz]). Table 3.1 is adapted from Table 5.6 in [33]. The original table has separate regression equations for siliciclastic and carbonate sediment types as well as expressions for a combined "All Sediments" sediment type. The general "All Sediments" regression equations are shown below. In the following tables, an R-squared

[b]The units of mean grain size are given as ϕ, a notation based on the Krumbein ϕ-scale. $\phi = -\log_2 \frac{D}{D_0}$, where D is the diameter of the grain in millimeters and D_0 is a reference diameter of 1 millimeter.

statistical metric is included which indicates how closely the core data fits the regression models.

Property	Regression	r^2
SSR	$1.164 - 0.3001(IOI) + 0.1253(IOI)^2$	0.97
η	$174.16 - 89.12(IOI) + 13.37(IOI)^2$	0.99
ρ	$1.02 + 1.21\ln(IOI)$	0.99
M_z	$17.9 - 6.0(IOI)$	0.84
k	$-3.31 + 4.33(IOI) - 1.38(IOI)^2$	0.22

Table 3.1: Index of impedance regression equations used for relating geophysical properties.

3.5.2 In Situ Regressions

Index of impedance regression equations were developed using 400 kHz acoustic waves, a much higher frequency than what is commonly used for sediment characterization. The experiments presented in Chapter 4 of this document use $5 - 20$ kHz acoustic signals. The IOI regression may yield inaccuracy when applied to mid-frequency data sets. Dispersive sound speeds in sediments have been observed, especially in sandy sediments. Sound speeds in the sediment are slower at low-mid frequency, a phenomena represented in the Biot-Stoll model. In [33] on p. 147, it is projected that the porosity, mean grain size, and sound speed will be overestimated and that bulk density will be underestimated when using measurements made at lower frequency.

For this reason, it is of interest to seek out another set of empirical regression equations with measurement frequencies closer to that of the Chapter 4 experiments. The empirical data set addressed in this section was collected

by a device known as the In Situ Sediment Acoustic Measurement System (ISSAMS). The device was used to measure compressional wave speed and attenuation after being inserted into the sediment. Pulsed sine waves of 58 and 38 kHz frequency were used to measure the time of flight and attenuation over multiple path lengths in the sediment. The device and its full capabilities are detailed in [56].

The regression equations provided in Table 5.4 in [33], and reproduced here in Table 3.2, were developed through measurements collected at 88 sites where the ISSAMS was deployed.[57] Plots of the data points and their associated regression lines are provided in Figures 5.7 and 5.9 in [33]. The regressions are to be used only within certain parameter value ranges where collected data informs a relationship, and not interpolated out of this range.

Property	Regression	r^2
Density	$\text{SSR} = 1.705 - 1.035\text{e}10^{-3}\rho + 3.664\text{e}10^{-7}\rho^2$	0.92
Porosity	$\text{SSR} = 1.576 - 0.015677\eta + 1.0269\text{e}10^{-4}\eta^2$	0.91
Mean Grain Size	$\text{SSR} = 1.190 - 0.03956M_z + 1.9476\text{e}10^{-3}M_z^2$	0.92
Density	$k = 0.00332e^{0.00241\rho}$	0.45
Porosity	$k = 2.153e^{-0.0401\eta}$	0.43
Mean Grain Size	$k = 0.697e^{-0.183M_z}$	0.52

Table 3.2: *In situ* regression equations relating geophysical properties.

Although these relations were developed using frequencies which are closer to those used in the SBCE and DISL experiments, the IOI regressions will be used because they can be calculated with remote measurements.

3.5.3 Other Regressions and Ad Hoc Relations

Another commonly referenced set of empirical regressions was developed in a series of articles by Hamilton and Bachman.[19,20,58–60] Their work surveyed the surficial sediment (top 30 cm) from the Bering Sea, the North Sea, the Mediterranean Sea, and other areas. These sediments are of various type and were gathered from diverse environments (e.g. continental shelf, continental slope, abyssal hill, and abyssal plain).

Hundreds of box and piston core samples were analyzed in a laboratory setting, often using a 200 kHz acoustic signal to measure sound speeds. Corrections were applied to the laboratory measurements so that the results would be representative of *in situ* characteristics. Corrections were applied to the temperature, pressure, and pore water salinity to meet a common set of conditions for measuring sound speed. *In situ* measurements were made at 14, 7, and 3.5 kHz. A summary of the measurement proceedure is provided on p. 145 of [33], and in detail throughout the series of articles, [19, 20, 58–60].

Besides the regressions presented in this chapter, ad hoc corrections to the Hamilton and Bachman regressions were published by the Applied Physics Laboratory at the University of Washington. The relations were published in the High-Frequency Ocean Environmental Acoustic Models Handbook, "TR-9407".[61] Those corrections were developed to improve acoustic model/data fits.[33]

Chapter 4

Sediment Characterization Experiments

4.1 Overview

Two experiments are reviewed in this chapter. Section 4.2 provides a brief introduction to the hardware and operational settings used to collect bottom loss data. Section 4.3 reviews the general method used for data processing. Each subsequent section of the chapter focuses on one experiment and contains background information, unique data processing methods, processed data, and results. The experimental data sets, and their respective ground truth measurements, were collected off of the New England and Alabama coastlines. The first data set was collected during the Seabed Characterization Experiment (SBCE) in 2017 over a region known as the New England Mud Patch. The second data set was gathered near the Dauphin Island Sea Lab (DISL). The experiment was conducted in 2017 off of the Alabama Gulf Coast in an area named Petit Bois Pass. Discussion of results presented in this chapter are found in Chapter 5.

4.2 Hardware

The Normal-Incidence Reflection Measurement System (NIRMS) is a self-contained bottom loss measurement apparatus which can be deployed independently or as an attachment to a CTD (Conductivity, Temperature, and Depth) device. NIRMS is a relatively simple system comprised of one source transducer, one receiving transducer, and an electronics package. The electronics package contains a power supply, data recorder, microcontroller, and all other components required to drive the source and recover data from the receiver. The source was used to output an LFM chirp centered at 12.5 kHz with a bandwidth of 15 kHz, sweeping from 5 to 20 kHz. The signal duration and repetition rate was set to 2 ms and 10 Hz, respectively. The receiving transducer is located at a known separation distance away from the source. The wavefront which propagates directly from the source to the receiver without surface or bottom boundary interaction is referred to as the "direct path signal" and is used as a relative reference to which any later received echo is compared. The recording device operated at a sampling rate of 96 kHz. Ship based GPS data was also recorded either by hand or by ship-board digital tracker, but is not integrated into NIRMS. NIRMS is an effective and simple tool for collecting bottom loss data which can be processed quickly to estimate sediment properties.

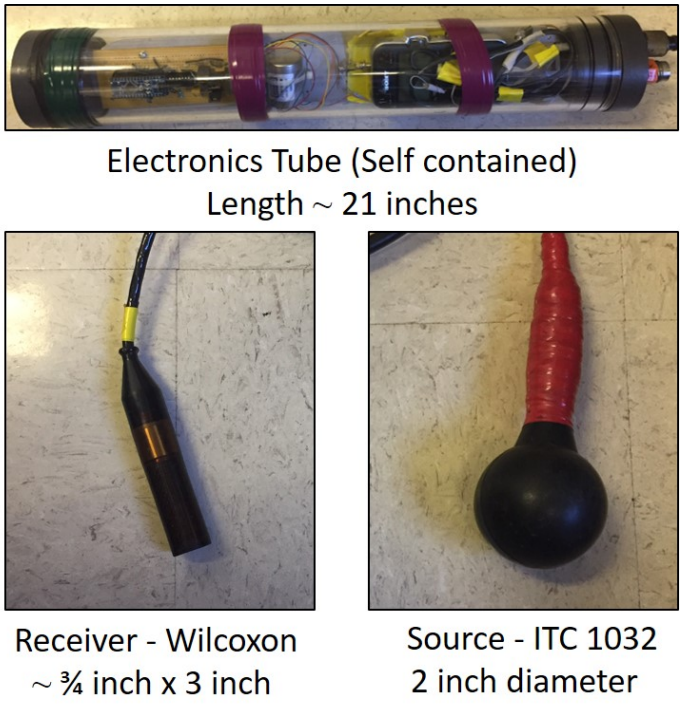

Figure 4.1: Photos of the electronics package, source, and receiver transducers of NIRMS, yet to be mounted. Photo credit: Michael Rukavina, Marcia Isakson

The source, receiver, and electronics package were harnessed onto a UniStrut frame and suspended by a tether, as seen in Figure 4.2. During SBCE, the NIRMS was attached to the frame of a CTD. For the DISL experiment, NIRMS was operated independently. The source is an ITC-1032 deep water omnidirectional transducer and the receiver is a Wilcoxon H507A hydrophone. Data sheets for the two transducers are included in Appendix B. The Wilcoxon H507A is a wide band hydrophone with a flat frequency response from 10 - 100,000 Hz and is generally omnidirectional except for some

attenuation in the backwards direction where the cable exits the device. The ITC 1032 source has a uniform directivity pattern at 10 kHz. The directivity patterns of both the source and receiver are of interest because on occasion the NIRMS can roll and pitch while in use. If the source and receiver were directional, the dynamic motion of the NIRMS would greatly affect the data. It is assumed that the roll of the device is minimal and that the source and receiver are on a horizontal plane above the seafloor.

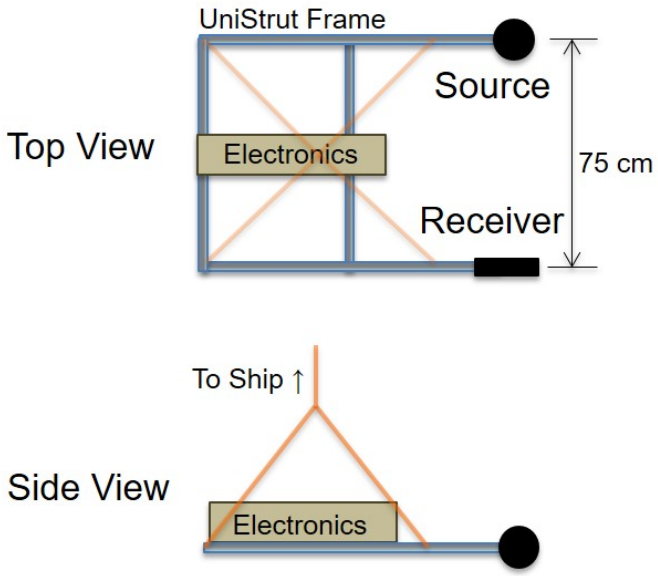

Figure 4.2: Plan and side views of the independently hoisted NIRMS. The distance between source and receiver is documented for each experiment and is pictured here as a 75 cm separation.

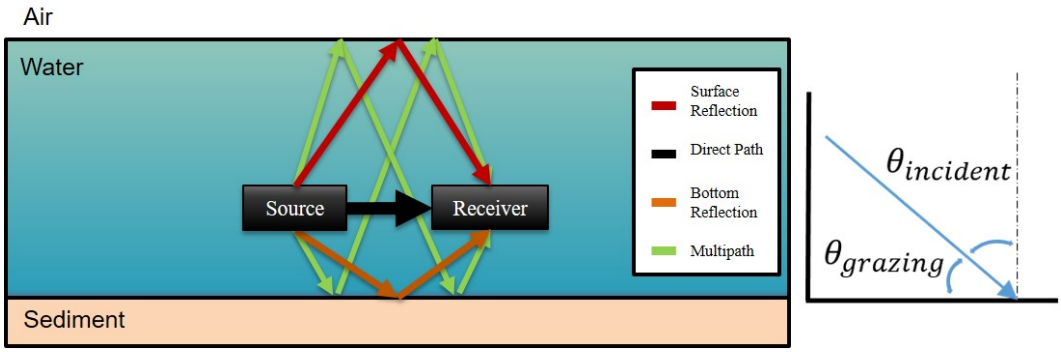

Figure 4.3: A cartoon representation of the bottom loss measurement apparatus in operation and the most significant acoustic propagation paths (left). The definition of incident and grazing angles (right).

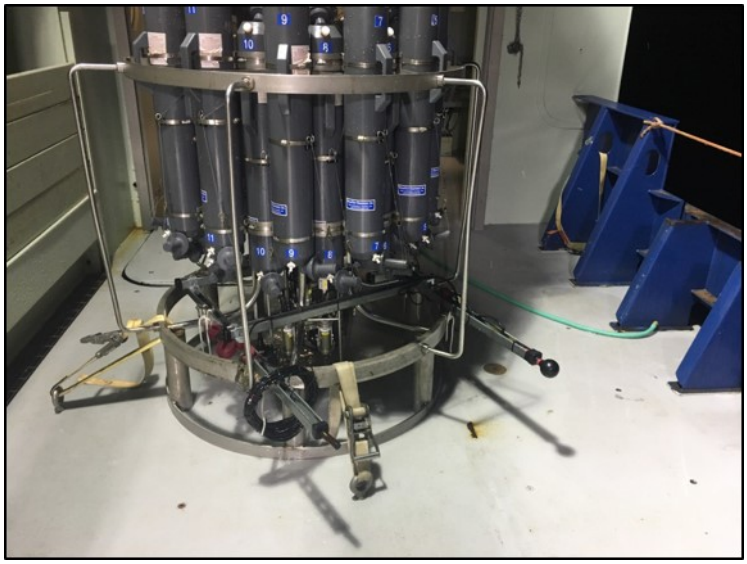

Figure 4.4: Bottom loss measurement apparatus attached to a SeaBird CTD device. The protruding source and receiver are located near the bottom of the CTD and cast identifiable shadows on the ground. Photo credit: Michael Rukavina

Figure 4.5: Bottom loss measurement apparatus independent of CTD. The braided cable in the picture supports the device, suspending it above the seabed in the water column. Photo credit: Marcia Isakson

4.3 Processing Method

The processing method described in this section was developed for near-normal incidence bottom loss data. The DISL data set, addressed in Section 4.5, explains unique processes when near-normal incidence cannot be assumed and when NIRMS is operated near the seafloor.

To begin, the audio files gathered during the field experiments were trimmed to eliminate portions prior to the NIRMS device being cast and after it had been retrieved. It was simple to do the trimming and cutting in a dedicated audio editing software and to save each cast as its own WAV file. For

each experiment, a representative direct path signal[a] was isolated and saved as a new audio file. These representative signals were used to build templates for the matched filtering operation. It is sufficient to use one representative direct path signal as the template rather than to dynamically define a new matched filter template for each ping, of which there can be tens of thousands per cast. Generally, each direct path arrival is very similar to the next so the benefit of redefining a new template is negligible. The trimmed data and representative pings were saved as WAV files in locations where the processing script will find and load them.

The data were loaded into Matlab and adjusted for any non-zero DC offset. The matched filter template was built by padding the representative isolated direct path signal with zeros so it is the same length as the cast data set which is being processed. The convolution process requires that the two functions exist over the same space. Recall that maximization of the system SNR occurs when the frequency response function of the matched filter template is the complex conjugate of the frequency domain representation of the signal of interest. The Fourier transform of the data set and the conjugate of the Fourier transform of the template were multiplied together, along with the bandpass filter. The absolute value of the inverse Fourier transform of that product is the output of the matched filter.

[a]By using a direct path signal recorded *in situ* as the matched filter template, the frequency response of the data recording system (e.g. source and receiver transducers, data acquisition system, cables, etc.) becomes nullified. If a synthetic matched filter template had been used then the response of the measurement chain would be ingrained in the output, making the bottom loss difficult to isolate.

Six frequency bands of interest were investigated: 5-20, 5-15, 5-10, 10-20, 10-15, and 15-20 kHz. Ship noise in the lower frequency bands (5-10 and 5-15 kHz) has artificially increased the bottom return. The bottom loss in the 5-10 kHz band is masked by this noise and therefore it is not reported in the tables below. The bandpass filter for each band of interest was applied during the matched filtering process. It is of interest to analyze the data in smaller bandwidths to investigate spectral nonuniformity in the reflected return.

With the absolute value of the matched filter output calculated, the significant peaks are reviewed to determine which ones indicate the direct path arrival, the reflection from the seabed, sea surface, or any other reflection path. Figure 4.11 illustrates the output of the matched filter. The location of the bottom return for each cast was documented. A time-bounded window was defined in order to automate the bottom loss calculation. The maximum return in this window is assumed to be the bottom reflection.

The pings are stacked side by side in order to visualize the reflectors in range and time. To do so, an algorithm was developed to find each maximum peak associated with the direct path and then to chop and align each ping, orienting them side by side in a 2-D matrix. Figure 4.12 shows one individual ping, oriented vertically. Each column represents a different ping in time and each row represents a sampled value, expressed as range in depth. A geometrical spreading loss correction was applied assuming a constant and known sound speed. The gain was applied to each row of the matrix proportional to the corresponding distance traveled by the pressure wavefront.

The absolute value of the matched filter output can be used to measure the BL, FWHM, and ratio of HWHM for each chirp. Outlier data were discarded and the mean and coefficient of variation of these metrics are reported. The BL was used to calculate a reflection coefficient, and subsequently used to the infer geophysical properties using the IOI regression equations provided in Chapter 3.

4.4 New England Mud Patch and the 2017 Seabed Characterization Experiment (SBCE)

4.4.1 SBCE Background

The Seabed Characterization Experiment was a multi-organization and multidiscipline research project which spanned three years. The survey sites of the SBCE are located 90-110 km south of Cape Cod, Massachusetts in an area with characteristically smooth bathymetry and small grain particles (e.g. silt, clay). This area is referred to as the New England Mud Patch (NEMP). In 2015 and 2016 pilot surveys were conducted; the surveys focused on subbottom profiling, bathymetric profiling, mud layer survey by gravity coring, surficial sediment collection by box core and multi-corer, as well as biological collection and taxonomy. More than 200 sediment cores were collected and analyzed by a multisensor core logger.

In situ acoustic measurements were collected by two devices. In 2016, data was collected by the Acoustic Coring System[16] (ACS) and in 2017, the Sediment Acoustic-speed Measurement System[62] (SAMS). The ACS had

acoustic transducers placed at the tip of a substrate penetrating nose cone which recorded flight times of acoustic signals as a function of penetration depth. The SAMS recorded flight times from a row of 9 linearly spaced sources to a receiving transducer that protruded into the soft sediment. Laboratory core data and *in situ* measurements are used for comparison and validation in this section.

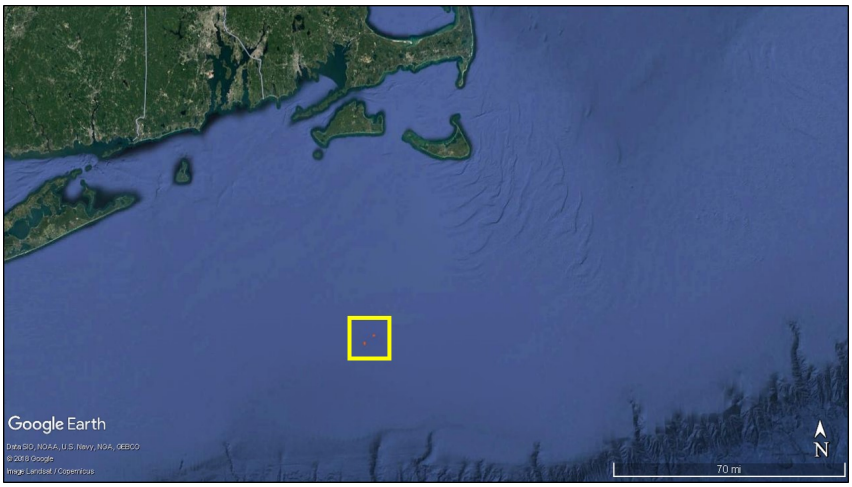

Figure 4.6: Google Earth satellite image shows part of the Northeast Atlantic Coast. A yellow box outlines the location of the NIRMS casts.

The main experiment took place in 2017; a large effort was undertaken to address acoustic propagation in fine-grained sediments and assess the performance of geoacoustic models and sediment characterization methods. The data sets presented in this section were acquired during the 2017 experiment by attaching acoustic instrumentation, NIRMS, to a SeaBird CTD. Outfitting CTDs with acoustic sensors is an opportunistic approach for acoustic data

collection and was achieved with only slight modification to the CTD frame, increasing the scientific value of each cast with minimal added cost.

Figure 4.7: The Normal-Incidence Reflection Measurement System, attached to CTD, shown on the dock in front of the Research Vessel Neil Armstrong. R/V Armstrong is operated by the Woods Hole Oceanographic Institute and supports both advanced research and the academic community. Photo credit: Michael Rukavina

The Research Vessel Niel Armstrong, partially pictured in Figure 4.7, conducted three casts of the NIRMS outfitted CTD over the course of the day on March 7, 2017. This resulted in the collection of approximately 105 minutes of acoustic data for processing.

The muddy surficial sediment was found to house a substantial amount of benthic infauna. Auxiliary tasks have been adopted to study the impact of

benthic biology on sediment acoustic properties.[63] Research on this topic is ongoing in both laboratory and field experiments.

4.4.2 SBCE Raw and Processed Data

Approximately 105 minutes of acoustic data was collected during three casts. There were issues staying within the dynamic range of the recorder during data acquisition. As the device was lowered to depth, the direct path reference signal increased in amplitude until it exceeded the dynamic range of the data acquisition system (clipped). This indicates either that the source or receiver, or both, operated more efficiently at higher hydrostatic pressure. Figure 4.8 shows each of the three casts and the sections which are utilized for analysis.

This is a challenge for data analysis because the bottom reflection is normalized to and dependent on the magnitude of the direct path. Because the direct path signal is clipped, its amplitude is underestimated by the recorded waveform and the calculated bottom loss could be underestimated.

All of the data whose direct path signal is clipped were discarded. For the few minutes where the device is stationary in the water column and the direct path signal is not clipping, the altitude of the device is 60 meters above the sea floor. Operating far away from the sediment interface may result in unaccounted-for attenuation and volumetric effects. The incident angle is very steep, less than 1 degree, and is assumed near-normal to the water/sediment interface.

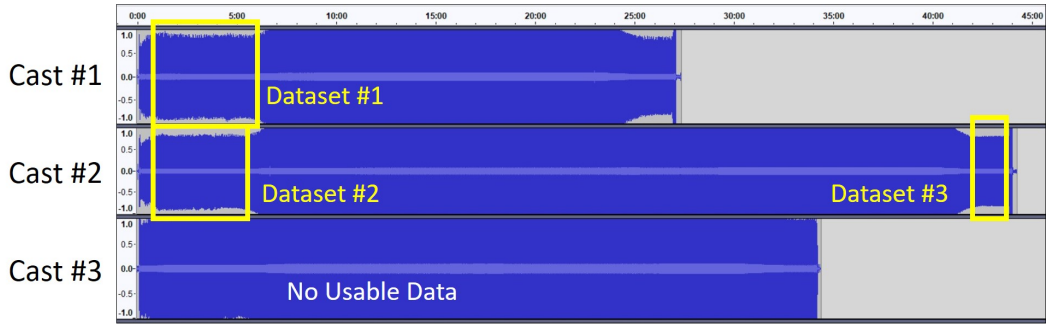

Figure 4.8: Raw time histories showing each cast and those non-clipped datasets used for analysis.

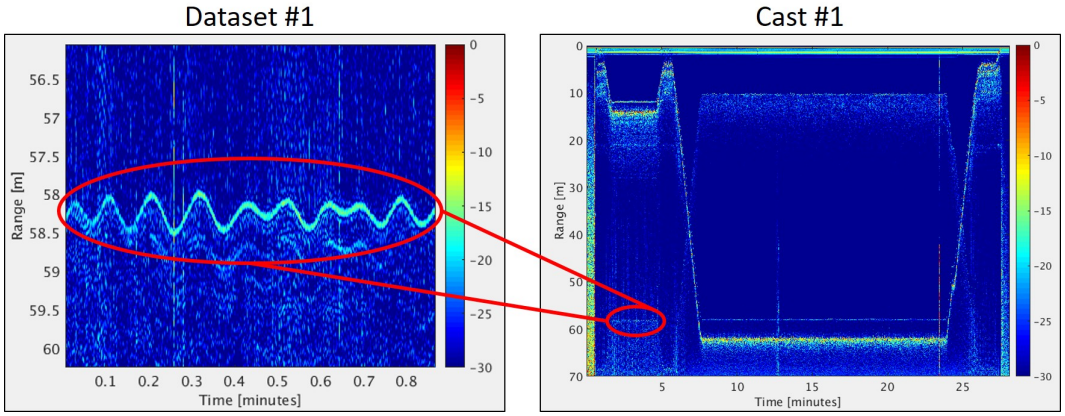

Figure 4.9: Visualization of Cast #1 (right), with zoomed section of non-clipped Dataset #1 (left).

The three datasets, shown in Figure 4.8, were windowed for processing and a representative direct path signal was isolated for use in the matched filter template for each. These direct path signals were used in the matched filter template and convolved with their respective data set. Each of the templates are similar and could likely be interchanged without much affect.

The following figures further motivate the need for the matched filtering process. In Figure 4.10, a snippet of raw data is plotted. Clearly, there are two major arrivals along with a smaller arrival near the 0.02 second mark. The two major returns are attributed to the direct path arrival. During operation, the source transducer outputs a chirp signal every tenth of a second. Direct path signals spaced by this repetition rate are predictably observed.

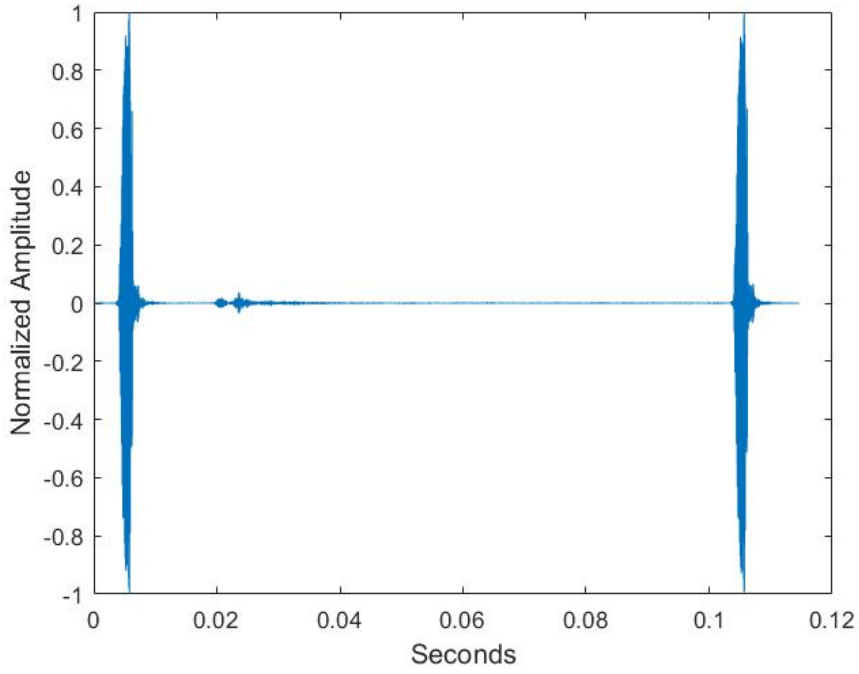

Figure 4.10: Data snippet showing two direct path arrivals. Data is normalized to the direct path peak amplitude.

Each significant acoustic reflector can be identified after the matched filter processing, provided some knowledge about the device's altitude in the water column. Significant peaks in the matched filter output are labeled in

Figure 4.11. This output highlights how the reflection from the seafloor is separable from background noise after matched filtering.

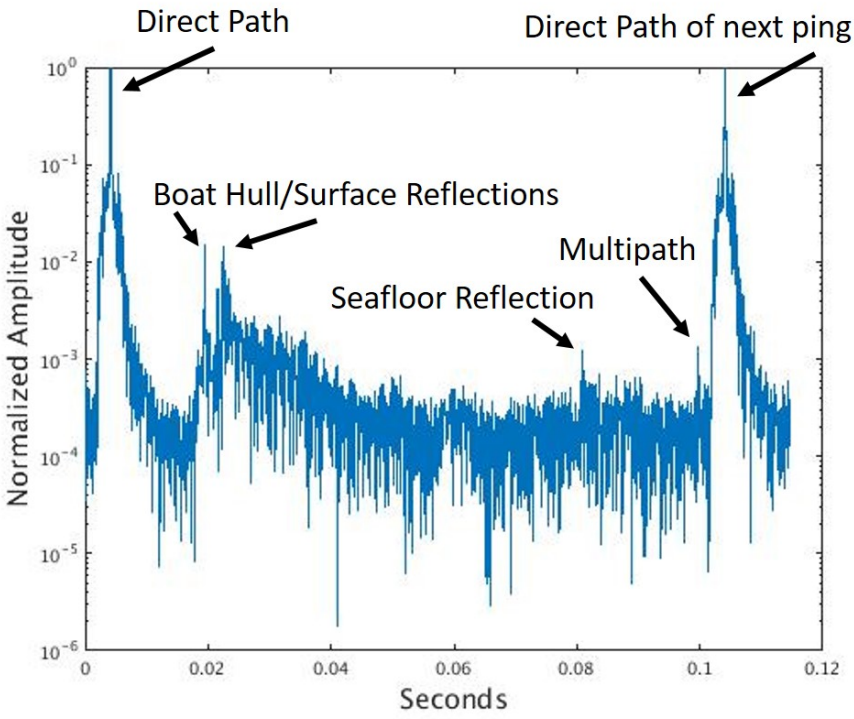

Figure 4.11: Matched filter output of the raw data provided in Figure 4.10 with labeled arrows indicating significant acoustic arrivals.

The matched filter output was split into single chirps, corrected for spreading loss, and plotted with a color mapping to indicate magnitude. The two-way travel time of each ping was translated into range and oriented vertically to provide an intuitive spacial picture of strong reflectors. Figure 4.12 displays one ping in this orientation. The bottom reflection can be seen near 58 meters in range.

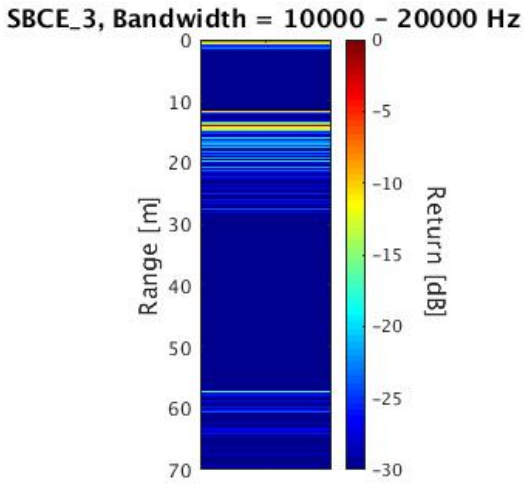

Figure 4.12: Bottom loss data from a single chirp

All chirps are aligned and stacked next to one another so that the environment can be observed as a function of depth-range and time. In Figure 4.13, the full range of data is provided in the left hand column and a bottom reflection zoomed version is presented in the right hand column. There exist artifacts of a secondary active sonar system which was operating during data collection. They are seen as red vertical lines in the plots below. The bandwidth of 10-20 kHz is presented here because it is the most representative of the complete data set, shown in Appendix A.1.

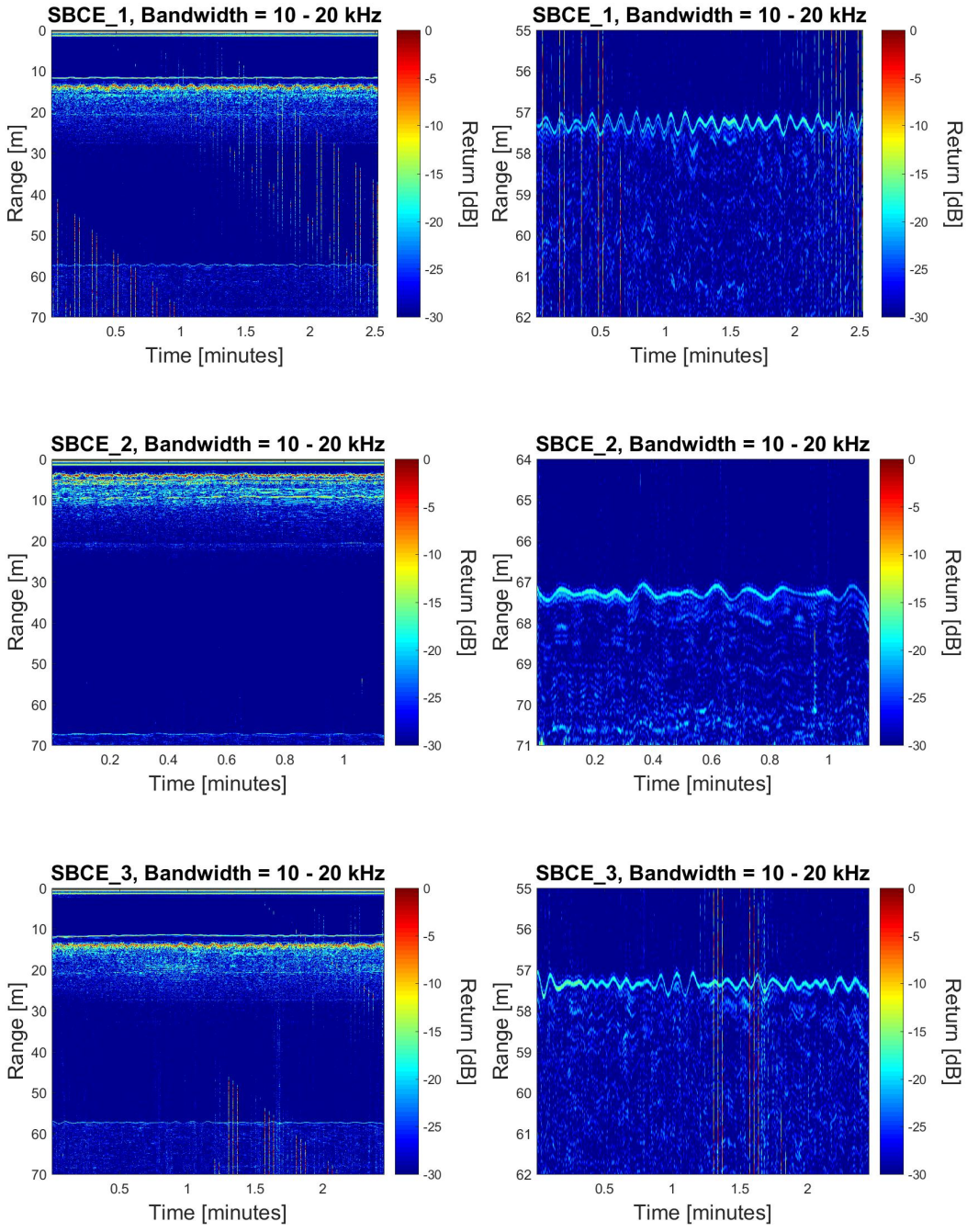

Figure 4.13: Bottom loss data, bandwidth = 10-20 kHz. Full depth record (left). Zoomed bottom reflection (right).

The values reported in the tables below show the mean and coefficient of variation for BL, FWHM, and the ratio of HWHM. Each metric was calculated after outliers had been discarded.

SBCE 1						
Freq [kHz]	BL Avg [dB]	BL CV [%]	FWHM Avg [ms]	FWHM CV [%]	HWHM Avg	HWHM CV[%]
10-15	15.9	34.7	0.226	53.5	1.17	14.7
10-20	18.2	34.8	0.103	26.9	1.55	22.0
15-20	19.0	52.3	0.313	49.8	1.14	21.9
5-15	13.4	44.3	0.098	59.8	1.52	35.5
5-20	17.3	37.9	0.070	31.5	1.98	40.7

Table 4.1: SBCE 1. Average BL, FWHM, and ratio of HWHM along with its coefficient of variation.

SBCE 2						
Freq [kHz]	BL Avg [dB]	BL CV [%]	FWHM Avg [ms]	FWHM CV [%]	HWHM Avg	HWHM CV[%]
10-15	19.5	35.9	0.237	52.7	1.16	17.7
10-20	19.0	37.3	0.112	22.4	1.45	19.2
15-20	17.6	39.8	0.305	12.5	1.03	14.9
5-15	15.0	47.7	0.101	68.9	1.50	49.4
5-20	18.6	36.4	0.055	44.4	2.28	42.9

Table 4.2: SBCE 2. Average BL, FWHM, and ratio of HWHM along with its coefficient of variation.

SBCE 3						
Freq [kHz]	BL Avg [dB]	BL CV [%]	FWHM Avg [ms]	FWHM CV [%]	HWHM Avg	HWHM CV[%]
10-15	16.1	41.5	0.253	26.4	1.20	13.3
10-20	17.7	30.1	0.145	14.6	1.42	17.4
15-20	18.8	41.9	0.284	22.5	1.17	13.0
5-15	12.7	48.4	0.118	22.1	1.44	28.4
5-20	16.6	33.4	0.069	28.8	1.83	32.7

Table 4.3: SBCE 3. Average BL, FWHM, and ratio of HWHM along with its coefficient of variation.

Application of the index of impedance regression equations yields frequency dependent estimates of geophysical properties. Those values for the largest bandwidth of interest (5-20 kHz) are reported in the table below.

***IOI* Regression, 5-20 kHz Bandwidth**			
Property	SBCE 1	SBCE 2	SBCE 3
Sound speed ratio, SSR [%]	0.987	0.985	0.988
Porosity, η [%]	77.4	80.2	75.9
Density, ρ $[g/cm^3]$	1.397	1.350	1.422
Mean grain size, M_z $[\phi]$	9.7	10.0	9.5

Table 4.4: Index of impedance regression equations used for relating geophysical properties, 5-20 kHz bandwidth.

4.4.3 SBCE Ground Truth

The NIRMS data was taken near a location referred to as the "Seep Site". The name stems from a suspected hydrocarbon seep in the area. A multicore logger measured a significant density and porosity gradient in the top 20 centimeters of surficial sediment. The density measurements range from

1.2 to 1.6 g/cm^3 and the porosity from 65 to 90 percent. The compressional wave sound speeds were reported to be nearly 1550 m/s, a SSR of 1.05. These numbers are interpreted from graphs published on the ARL Seabed Characterization Experiment website.[64]

The Acoustic Coring System (ACS) was deployed seven times, the nearest deployment of the ACS to the Seep site was named AC-1. The sound speed was measured as a function of depth and shows a downward trend over the first 1.5 meters depth and an upward trend below that. The sound speed is reported to be between 1475 and 1450 m/s, a SSR between 0.98 and 1.00. In further detail, [16] displays and compares all of the collected data and shows a frequency dependence of the sound speed, also as a function of depth. The SSR is lower for lower frequencies, and increases at depths greater than 50 cm. At 25 kHz with a depth of 50 cm the SSR is reported as 0.955 to 0.985. The porosity data was clustered around 60% and the mean grain size varied between 10 to 100 μm ($\phi = 7$ to 4).

The porosity and mean grain size values depended on how sandy or muddy each area was and AC-1 was more muddy than other sites. The sediment nearest to where NIRMS data was collected is predominately small silt and clay sized particles which make up a porous sediment suspension. The structure is often compared to a house of cards where the small grains act as a saturated lattice, supporting organic matter and sparse sand grains throughout. The mud layer in this region is approximately 12 meters thick. Figure 2.8 in [8] shows this clay structure as observed by scanning electron microscopy.

4.5 Dauphin Island Sea Lab Experiment (DISL)

4.5.1 DISL Background

The Dauphin Island Sea Lab Experiment was a collaborative research project between the Applied Research Laboratories at the University of Texas at Austin and the Dauphin Island Sea Lab conducted in May of 2017. The field experiment site is located between Dauphin Island, AL and Petit Bois Island, MS at an inlet named Petit Bois Pass. Three types of experiments were conducted including the gathering and analysis of core[10] and grab samples, *in situ* sediment acoustic measurement,[65] and bottom loss measurement by NIRMS.

Petit Bois Pass was selected as a field experiment site to investigate effects of infauna on the geoacoustic properties of sediments. The presence of infauna challenges sediment characterization models with the dynamic processes of bioturbation and resulting heterogeneity.[66,67] Burrowing organisms restructure the sediment, building a framework of tubes and voids while depositing organic material. Sonar chirps affected by the varied sediment structure and biological ecosystem may confound traditional characterization models. Figure 4.14 is an example of a hard tube structure created by burrowing infauna.

Figure 4.14: A shelly tube structure obtained by surficial sediment grab sample by the R/V Pelagia. Photo Credit: Michael Rukavina, Marcia Isakson

The bottom loss measurement apparatus was deployed 22 times over the course of two days, May 8-9, resulting in the collection of nearly 4 hours of recorded data. The experiment location is shown in Figure 4.15 with the operating area boxed in yellow, within which are orange lines representing the GPS position of the R/V Pelagia during those two days. Figure 4.16 is further zoomed in to Petit Bois Pass; overlayed on the image are black and white markers indicating the GPS location of the R/V during the collection of bottom loss data. Three sites have been defined to simplify the ground truth comparison.

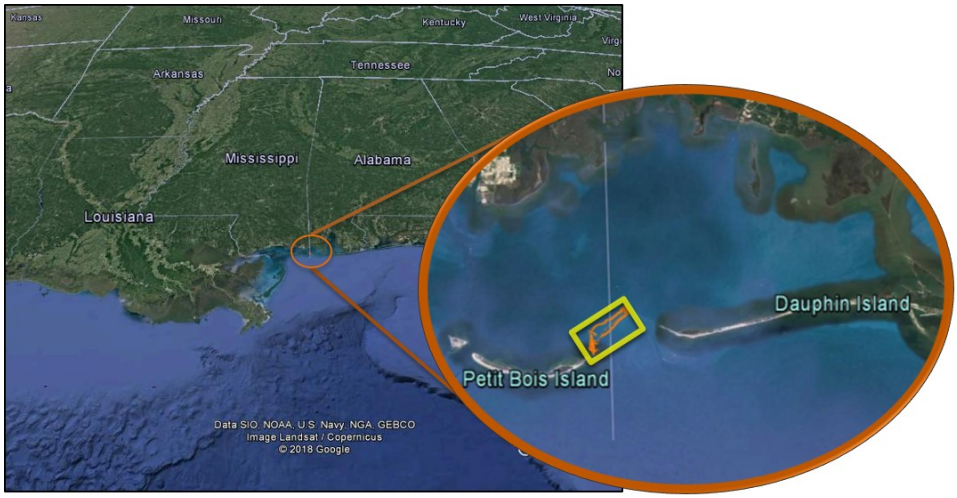

Figure 4.15: Petit Bois Pass, located off of the Gulf Coasts of Alabama and Mississippi between Petit Bois Island and Dauphin Island. The yellow box outlines the R/V Pelagia GPS locations, shown in orange.

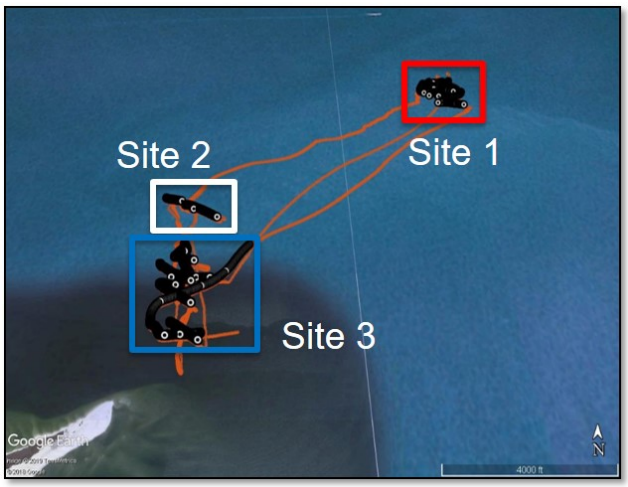

Figure 4.16: Zoomed view of Petit Bois Pass. R/V Pelagia GPS location are shown in orange and overlayed on those tracks are black and white markers indicating the GPS location of the vessel while bottom loss data was being collected. Three sites are defined for easy comparison to ground truth data.

Fourteen total core samples were collected from sites #1 and #2 and then analyzed in the laboratory using a new tool, the Core and Resonance Logger.[10] The core logger uses a pitch-catch method to determine sound speed and attenuation in a high frequency regime (100 to 300 kHz), and a resonance method to determine sound speed in a low frequency regime (8 to 23 kHz). After the acoustic experiments were finished, the cores were segmented by depth and analyzed for porosity, grain size, and biodensity.[10,68] The *in situ* sediment acoustic measurements were made using a variant of the ACS. The variant apparatus used the same type of compressional and shear wave transducers except they were deployed on a stationary frame and inserted into the sediment independently from any coring device.[65] The apparatus measured compressional and shear wave speeds along with acoustic attenuation at sites #1 and #2.[10,65,68]

4.5.2 DISL Processed Data

The water column depth in Petit Bois Pass is shallow, between 5-15 meters. Preliminary analysis of the DISL bottom loss data revealed that NIRMS was operated near the seafloor, sometimes within 2 or 3 meters. Three possible repercussions are addressed.

First, spherical wave effects can affect the measured reflection coefficient. Because the reflection coefficient is dependent on angle, a spherical wavefront doesn't reflect uniformly and the reflection becomes a distorted semi-spherical wave.[69] These effects cause errors between models and data

measurements taken near the interface at small grazing angles, especially below and near the critical angle. One resulting phenomena is known as the head wave or lateral wave. This occurs when part of the wavefront is incident at the critical angle, propagates along the fast interface and back out into the water column. The lateral wave can interfere with the specular reflection. A visual example is shown in Figure 1 in [69]. At grazing angles larger than 50 degrees, the spherical wave model, plane wave decomposition model, and plane wave fluid model are all in good agreement. Spherical wave effects are not considered in this experiment.

Secondly, temporal side lobes in the matched filter output of the direct path signal may interfere with the main lobe of the bottom reflection when operating near the water/sediment interface. The removal of the direct path in the matched filter output results in a better estimate of bottom loss when side lobe interference occurs. If there is no interference, this process has no affect on bottom loss values. The lobe structure of the direct path was isolated by matched filtering the template with itself. The direct path contribution is then subtracted from the total bottom loss data.

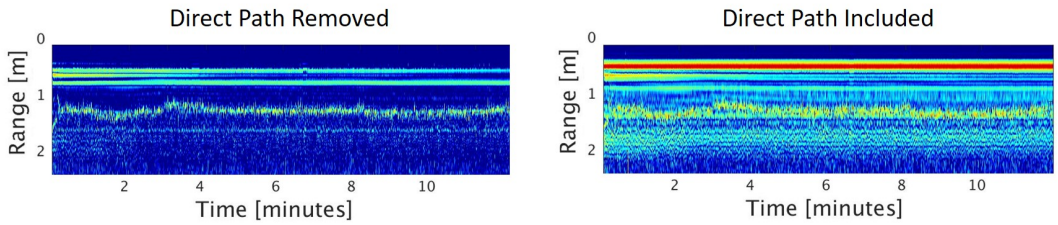

Figure 4.17: Bottom loss data collected near the water/sediment interface requires direct path removal. The reflected return is visible near the 1.2 meter range.

Lastly, the assumption of near-normal incidence is not appropriate. Figure 4.18 shows the distribution of incident angles at each of the three sites. Without measurement of a near-normal reflection, the characteristic impedance of the sediment becomes undetermined in the analytical model.

The incident angle of each ping was calculated using two known parameters. The first parameter is the separation distance between the source and receiver. The separation distance for both days of the experiment was documented as 0.75 meters. Second, the speed of sound in the water column was measured to be nearly 1515 m/s, recorded in [65]. With knowledge of the separation distance and the speed of sound, one can calculate the time of flight for the direct path. Next, the delay between the direct path and the bottom bounce path is determined. The total time of flight for the bottom bounce path is a summation of the direct path flight time and the observed delay time. The inverse sine of the ratio of direct path time of flight and bottom bounce time of flight was used to determine the incident angle. The incident angle can heavily influence the magnitude of the reflection, especially near the

angle of intromission. Based on ground truth measurements reported later in this chapter, an intromission angle of 70 degrees incidence is expected. The experimental measurement angles are below this angle.

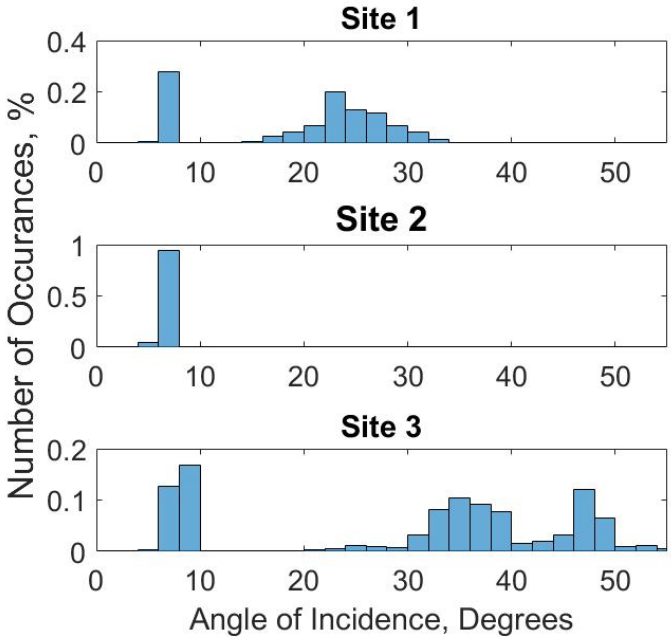

Figure 4.18: Angle of incidence for DISL sites #1, #2, and #3. Sites #1 and #2 will be analyzed using a parameter space search procedure to determine sediment physical properties.

The reflection coefficient shown in Eq. (3.5) can be rearranged to remove the dependency on the transmitted angle, θ_t. The trade-off is a loss of generality for the impedance of the sediment. The impedance term is assumed to be the product of sound speed and density, $Z_2 = \rho_2 c_2$. By application of Snell's Law, the transmitted angle can be expressed in terms of the incident

angle,[41]

$$\cos(\theta_t) = \sqrt{1 - (c_2/c_1)^2 \sin^2(\theta_i)}. \tag{4.1}$$

The result is the Fresnel reflection coefficient, shown on p. 62 in [70],

$$R = \frac{\frac{\rho_2}{\rho_1}\cos(\theta_i) - \sqrt{\frac{c_1}{c_2} - \sin^2(\theta_i)}}{\frac{\rho_2}{\rho_1}\cos(\theta_i) + \sqrt{\frac{c_1}{c_2} - \sin^2(\theta_i)}}. \tag{4.2}$$

The Fresnel reflection coefficient is calculated over a 2-D parameter space, defined by bulk density ratio and sound speed ratio. Within the parameter space the least-square residual between the analytical and experimentally measured reflection coefficients were summed for each chirp over all respective incident angles. The resulting minimum identifies an angle-independent estimate of the two parameters.

In the figures below, bottom loss data are analyzed by parameter space search. All data, both oblique and near-normal incidence data are used in this method. Figure 4.19 includes all data from all sites. Site #2 does not have it's own parameter space search result because the data was collected at a uniform incident angle and the parameter space search requires a diverse range of input angles.

Six frequency bands of interest are displayed. Red regions in Figures 4.19, 4.20, and 4.21 represent the smallest of the least-square residual. The blue space represents data which is more than 1% greater than the residual minima. Two clusters of minima per plot are observed. This ambiguity exists because the absolute value of the analytical reflection coefficient was

used to calculate the residuals. The residual minima representing a negative reflection coefficient, found generally in the bottom left, are ignored for practical purposes.

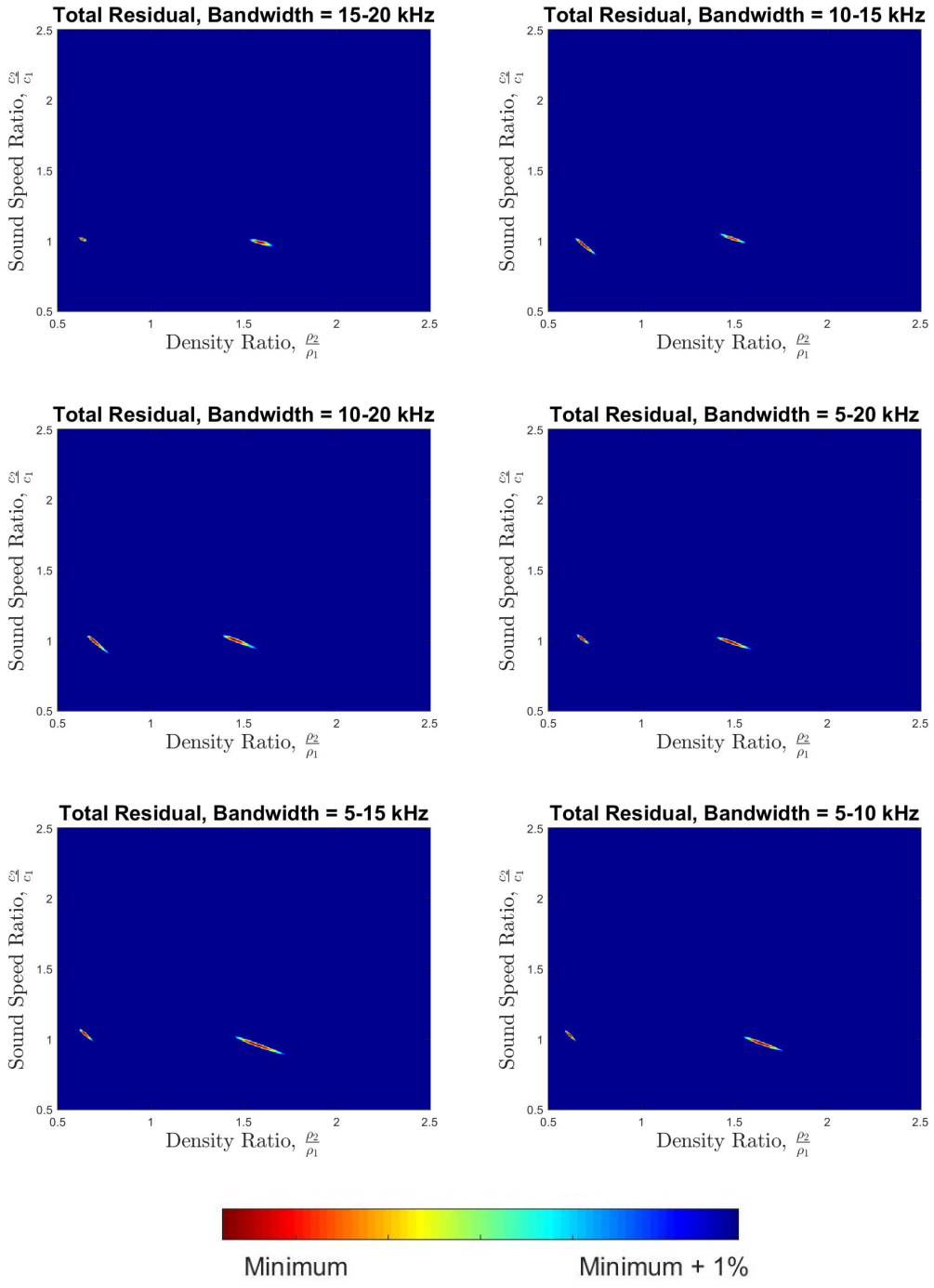

Figure 4.19: Combined all DISL data from sites #1, #2, and #3, minimum residuals for each bandwidth of interest.

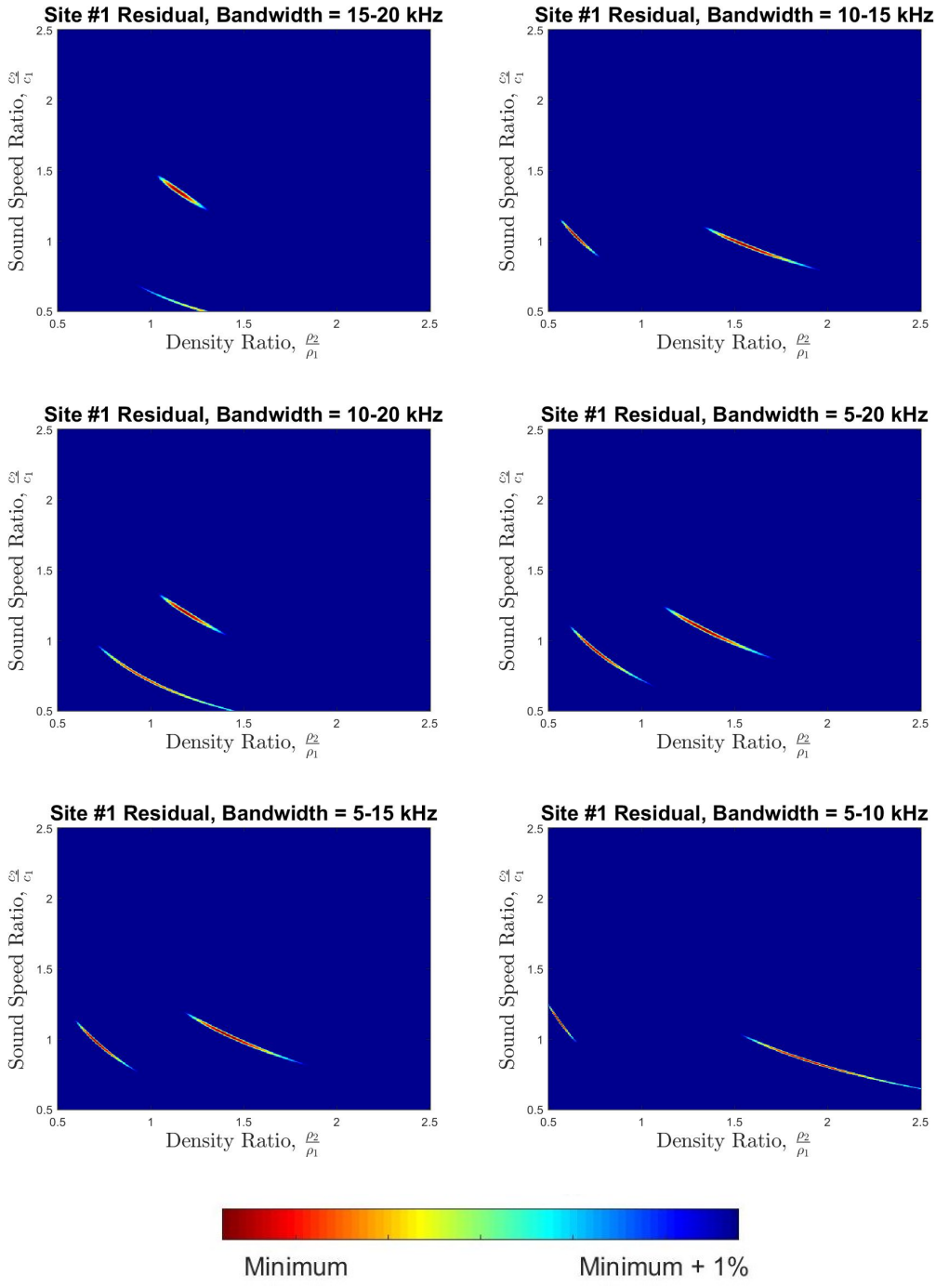

Figure 4.20: DISL site #1, minimum residuals for each bandwidth of interest.

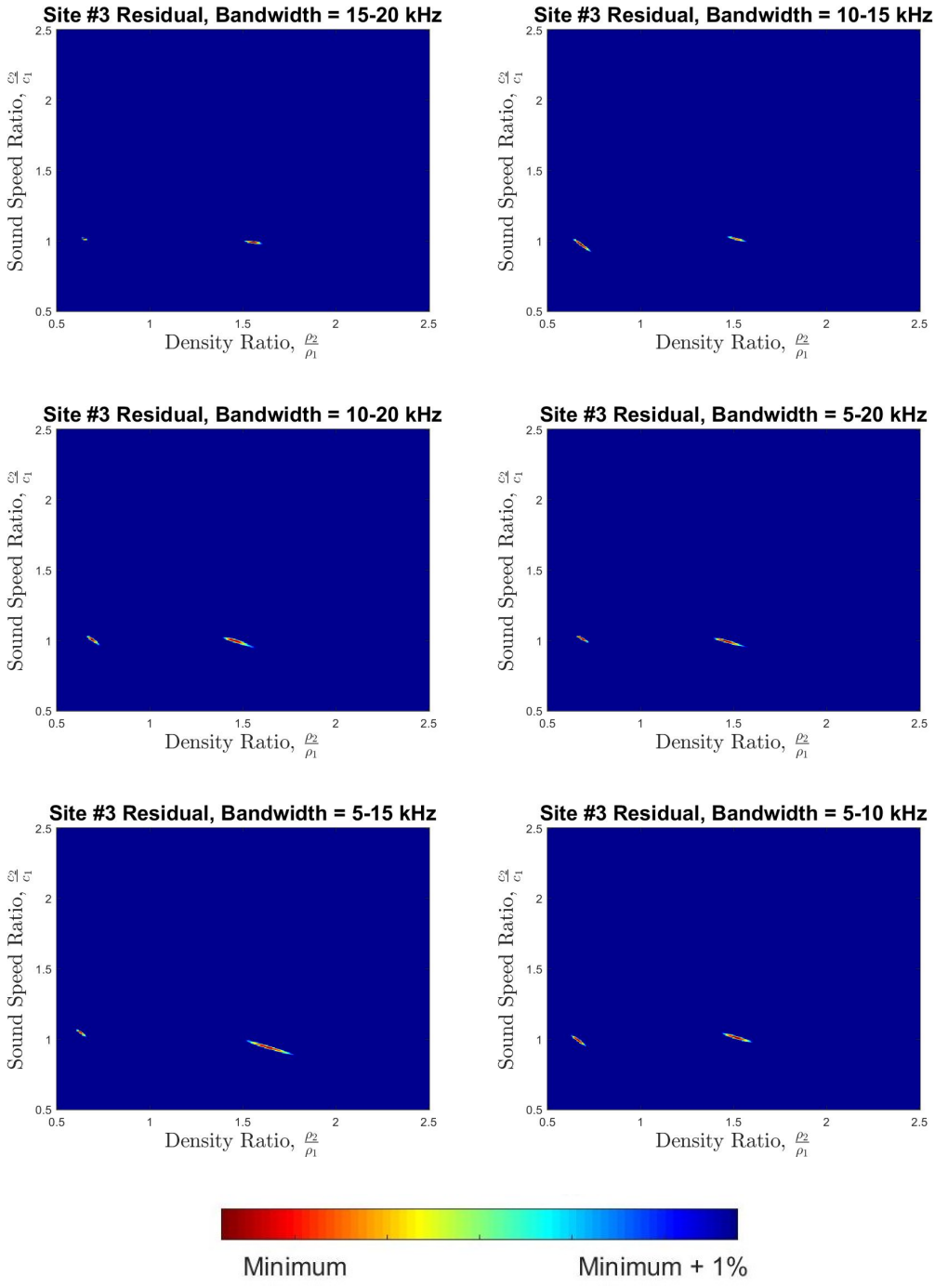

Figure 4.21: DISL site #3, minimum residuals for each bandwidth of interest.

The parameter space search yielded an estimate for sound speed and density ratio corresponding to the location of a minimum in the sum of least-squares residual. Tables 4.5 and 4.6 list results for the residual minima for each frequency band at sites #1 and #3.

Analysis of the parameter space accuracy was conducted by considering error contours of the residual. The error contours are defined with respect to the minima and increase by a percentage of the minima. For example, the 10% contour envelops an area within which the residual does not exceed 1.1 times the minima. Tables 4.5 and 4.6 include error contour percentages which indicate at what contour the ground truth measurements exist in the parameter space.

Parameter Space Search Results, Site #1			
Frequency	Density [ρ]	Sound Speed Ratio	Error Contour
5-20 kHz	1.36	1.09	40%
10-20 kHz	1.81	1.21	36%
15-20 kHz	1.19	1.36	5%
5-15 kHz	1.34	1.14	45%
10-15 kHz	1.62	0.97	28%
5-10 kHz	1.93	0.86	14%

Table 4.5: Parameter space search results, site #1

Parameter Space Search Results, Site #3			
Frequency	Density [ρ]	Sound Speed Ratio	Error Contour
5-20 kHz	1.50	1.00	39%
10-20 kHz	1.50	1.00	29%
15-20 kHz	1.61	0.99	20%
5-15 kHz	1.68	0.95	27%
10-15 kHz	1.55	1.02	13%
5-10 kHz	1.55	1.02	18%

Table 4.6: Parameter space search results, site #3

The BL, FWHM, and ratio of HWHM metrics are provided below in Tables 4.7, 4.8, and 4.9. The values were calculated in the same way as in the SBCE data. Outliers were discarded and bottom loss were averaged using their linear values prior to calculating the dB values.

DISL 1						
Freq [kHz]	BL Avg [dB]	BL CV [%]	FWHM Avg [ms]	FWHM CV [%]	HWHM Avg	HWHM CV[%]
10-15	13.5	53.2	0.170	68.2	1.33	33.8
10-20	13.8	58.3	0.097	66.3	1.54	31.5
15-20	12.9	58.3	0.163	75.8	1.23	31.2
5-10	15.0	49.6	0.237	68.5	1.20	42.0
5-15	14.2	53.8	0.085	57.0	1.58	31.3
5-20	14.1	56.0	0.067	67.9	1.89	35.6

Table 4.7: DISL 1. Average BL, FWHM, and ratio of HWHM along with its coefficient of variation.

DISL 2						
Freq [kHz]	BL Avg [dB]	BL CV [%]	FWHM Avg [ms]	FWHM CV [%]	HWHM Avg	HWHM CV[%]
10-15	13.7	47.3	0.238	43.7	1.22	13.3
10-20	15.1	48.7	0.120	52.9	1.37	18.4
15-20	15.4	52.2	0.227	69.6	1.18	18.6
5-10	11.8	37.7	0.346	34.3	1.24	21.0
5-15	13.2	37.4	0.112	28.1	1.43	18.7
5-20	14.7	44.0	0.076	50.4	1.68	26.5

Table 4.8: DISL 2. Average BL, FWHM, and ratio of HWHM along with its coefficient of variation.

DISL 3						
Freq [kHz]	BL Avg [dB]	BL CV [%]	FWHM Avg [ms]	FWHM CV [%]	HWHM Avg	HWHM CV[%]
10-15	12.7	53.6	0.159	74.8	1.35	27.9
10-20	14.0	58.1	0.099	75.8	1.62	36.8
15-20	13.7	64.7	0.165	84.9	1.33	34.9
5-10	14.8	66.3	0.238	87.2	1.08	37.1
5-15	13.5	55.6	0.079	73.5	1.60	39.1
5-20	14.3	54.0	0.074	62.1	1.90	48.0

Table 4.9: DISL 3. Average BL, FWHM, and ratio of HWHM along with its coefficient of variation.

Each of the three sites had some amount of data that was collected at near-normal incidence. Casts whose data was collected with an average angle of incidence less than 10 degrees was assumed to be near-normal. Three casts at each site qualify as near-normal incidence by this definition. The IOI regressions for the 5-20 kHz bandwidth are documented in the table below. The IOI is based on average near-normal incidence bottom loss numbers for each of the three sites. They were calculated as 13.4, 14.7, and 14.0 dB for

sites #1, #2, and #3, respectively. A portion of near-normal bottom loss data plots are provided in Appendix A.2.

***IOI* Regression, 5-20 kHz Bandwidth**			
Property	DISL 1	DISL 2	DISL 3
Sound speed ratio, SSR [%]	1.001	0.993	0.997
Porosity, η [%]	66.8	71.4	69.0
Density, ρ $[g/cm^3]$	1.572	1.465	1.503
Mean grain size, M_z $[\phi]$	8.4	9.0	8.7

Table 4.10: Index of impedance regression equations used for relating geophysical properties, 5-20 kHz bandwidth.

4.5.3 DISL Ground Truth

Ground truth data was collected by *in situ* acoustic measurement and core samples. The ground truth data was reported in [10,65,68]. The cores and acoustic measurements were conducted at sites #1 and #2 where the presence of infauna was expected. Site #3 does not have ground truth measurement data, however it is known that there was less benthic biology at this site. The tables below represent measurements from the top 20 cm of surficial sediment.

The *in situ* compressional wave measurements were conducted with 100 kHz acoustic signals. The data were collected at depths between 0 and 25 cm. The bottom water sound speed was estimated by CTD measurement to range from 1512-1522 m/s. A water sound speed of 1515 m/s was used in the NIRMS analysis. Figure 4 in [65] provides the full detail of SSR, attenuation, porosity, and mean grain size of sites 1 and 2[b]. After the acoustic measurements

[b]Site 1 in this document is referred to as Site 3 in Figure 4 of [65].

were recorded, diver cores were obtained and taken for laboratory analysis of porosity and grain size distribution. Some of the samples were sieved to collect infauna for further study.

***In situ* Acoustic Measurements, 100 kHz**		
Property	DISL 1	DISL 2
Sound speed ratio, SSR [%]	1.05	1.02
Porosity, η [%]	60	64
Density, ρ $[g/cm^3]$	1.70	1.63
Mean grain size, M_z $[\phi]$	4	4

Table 4.11: *In situ* acoustic sound speed measurements along with core sample measurements of porosity, density, and grain size from [65].

Cores collected at sites #1 and #2 were analyzed using a core and resonance logger. The device operated in either a pitch-catch mode, or a resonance mode. The range of acoustic frequencies for each mode are 100-300 kHz and 8-23 kHz, respectively. Both modes of operation yielded similar results, shown below in Table 4.12.

Core Logger Acoustic Measurements		
Property	DISL 1	DISL 2
Sound speed ratio, SSR [%]	1.04	1.03
Porosity, η [%]	60	62
Density, ρ $[g/cm^3]$	1.71	1.64
Mean grain size, M_z $[\phi]$	3-5	4

Table 4.12: Acoustic core logger estimate of sound speed along with measurements of porosity, density, and grain size from [10].

An effort was made to compare the sound speed in the sediment to the total amount of biomass recovered after sieving. At site #2, an area with

greater amounts of biomass, the sound speed ratio increased by approximately 5%, and porosity increased by 14%. These findings were unexpected because as porosity increases, the sound speed is expected to approach that of water. The mean grain size was also found to increase with increasing biomass. Benthos can consolidate fine grains through habitat construction or digestion. Although the data set is limited, it was observed that a high spatial density of hard worm tubes occurred in the surficial sediment where porosity and mud content was low. In areas with large amounts of infauna, increased variability in measured sound speeds were observed.

Chapter 5

Discussion and Conclusions

5.1 SBCE Discussion

The metrics reported in Tables 4.1, 4.2, and 4.3 show a frequency dependence with consistent trends among all sites. The greatest bottom returns occur in the lowest frequency bands of interest, 5-10 and 5-15 kHz. However, these returns are artificially increased due to noise from the research vessel. The noise is visualized as vertical bands of high intensity returns in Figures A.2 and A.3. The 5-10 kHz bandwidth was excluded from the analysis because the bottom reflection is masked by this operational ship noise. Possible sources of this noise include the gearboxes and electric motors which the R/V Armstrong uses in its multi-drive, low-voltage diesel electric propulsion system.

The bottom reflection in the 5-15 kHz band was able to be measured more consistently, but again the ship noise artificially increased the total average return. This band has a relatively large coefficient of variation. The CV is 6 to 8% greater than the CV in all other bands, with one exception. This indicates that fluctuating background noise levels contributed to an increased variance in bottom loss measurements.

The 10-20 kHz bandwidth is considered the most representative fre-

quency band of interest in this experiment because it is the widest band in which the extraneous noise is suppressed. The index of impedance regression equations estimate a 0.985 sound speed ratio. Shown in Figure 8 of [16], *in situ* measurements at a nearby location recorded an SSR between 0.985 and 1.0 in the top-most sediment, reducing to 0.985 at 20 cm depth. This is a promising result for the application of IOI regressions for predicting sound speeds using 10-20 kHz normal incidence bottom loss data. Multi-sensor core logger sound speed measurements are also included in Figure 8 of [16], and they are generally in agreement with the acoustic coring system.

Like the BL metric, the FWHM and ratio of HWHM also show a consistent trend in frequency dependence. The largest FWHM and smallest ratio of HWHM are attributed to the 15-20 kHz band. As was shown in Section 2.3, it is expected that the FWHM increases as the bandwidth is decreased and vice versa. The difference in pulse width between the 10-15 and 15-20 kHz bands is unexpected and could be attributable to frequency dependent volume scattering or density gradient effects.

At large grazing angles, acoustic energy will penetrate into the sediment and then reflect off of volume inhomogeneities and impedance gradients. Bioturbation in the surficial sediment can contribute to both inhomogeneities and gradients, thus increasing bottom loss variability. The benthos who live in the New England Mud Patch are numerous and diverse in their affect on bottom loss.[63] During a pilot study in 2015, infauna abundance was measured and then classified for acoustic significance. Significant acoustic traits

included body size, body type, and sediment activity. The greatest abundance of infauna was found at the Seep site where NIRMS data was collected, nearly 150 infauna per square meter. Of those, 46.7% were hard-bodied and 24.2% were structure building. Figure 11 in [63] provides a chart detailing the abundance, body type, and sediment activity of the animals. The most acoustically relevant benthos were brittle sea stars (amphiurid), crustacea (tanaeid), and structure building worms (maldanid). Impedance gradients, bioturbation, and other volume effects are difficult to separate from surface scattering mechanisms. Often, a time-domain window is used to isolate the early interface reflection from later volume-based returns, as was done in this analysis.

Those data which were not saturated with noise show sub-bottom reflections which are correlated with the shape of the interface reflection. One explanation could be the existence of an impedance gradient in the uppermost sediment. The range delay of the correlated returns indicate that the thickness of the suspected top gradient is approximately 0.5 meters. If the sub-bottom reflections were a consequence of layering, their shape would not be correlated with the shape of the interface reflection. Those returns that are not correlated with the surface return, and are not consistent enough to indicate layering, are attributed to sub-bottom reflectors such as large shells or rocks.

The IOI density regression equation estimated an average density of 1.36 g/cm^3 across the three datasets. Ground truth measurements described in [16] used two means of determining bulk density; the results varied depending on the measurement method. A gamma-ray attenuation method measured a

range from 1.3 to 1.58 g/cm^3 in the uppermost sediment. A traditional dry weight measurement procedure was used to calculate the wet sediment bulk density of 1.4 to 1.58 g/cm^3 in the uppermost sediment. In Section 3.5.2, it was predicted that the bulk density would be underestimated. The IOI regression resulted in an estimate which fell inside the range of reported ground truth measurement for the gamma-ray attenuation method, although it was on the lower end of the range. The regression estimate is approximately 10% lower than the median core logger density.

Other geophysical properties such as porosity and mean grain size also follow the trends predicted in Section 3.5.2. The porosity and mean grain size are expected to be overestimated. At this time there are no low to mid frequency corrections for these empirical relations. The porosity estimate from IOI regression equations averaged to 79.6%. This is an overestimation of almost 20% compared to measurements provided in [16] which clusters around a porosity of 60%. However, measurements gathered by a multi-core logger[64] reported porosity values up to 90%.

Because the sediment density was slightly underestimated, it is logical that the porosity would be overestimated. And in order to increase the porosity, the mean grain size parameter, ϕ, must become larger. The mean grain size was estimated to be nearly $\phi = 10$. This is equivalent to a 1 micron diameter grain, inconsistent with the actual size of an average particle. In [8], a scanning electron microscope did observe clay particles which had dimensions smaller than a micron, but the mean grain size was reported as approximately

$\phi = 6$. This corresponds to a medium/fine silt with a diameter of 16 microns. The laboratory measurement of the core samples reported a mean grain size of $\phi = 4$. Therefore, for this study, the mean grain size regression equation is not accurate when applied to low frequency data.

Overall, the sound speed estimate was very close to ground truth measurement. It is generally accepted that muddy sediments can have sound speeds that are less than that of the overlaying water. Thus from sound speed measurement it is possible to estimate that the sediment in the NEMP does indeed have significant mud content. However, the density estimate should be refined. An argument could be made that the density estimate should be increased by 10% when using IOI regressions at lower frequencies, but more data is required for robustness. For poroelastic sediments, low density estimates from reflection measurements are common.[40] This is especially common for sandy sediments, but it is less clear how this applies to mud.

5.2 DISL Discussion

The DISL experiment gathered a large amount of usable data for analysis. The unique challenge was that much of the data was not taken at near-normal incidence. To overcome this challenge, a parameter space search was conducted as a simple inversion method. The parameter space search used the sum of least squares to find a minimum residual between experimental data and the angle-dependent analytical fluid model over a prescribed parameter space. The minimum residual in this space identified a set of parameters, density and

sound speed ratios, as the inputs to the model which most nearly matched the experimental measurements. Data measured at near-normal incidence were analyzed both in the parameter space search and by IOI regression.

Figures 4.20 and 4.21 show the results of the parameter space search for sites #1 and #3. Site #2 does not have its own inversion results because there is no variety of incident angle, but this site is included in the combined residual in Figure 4.19. Red regions in these plots represent minima of the residual in the parameter space. Two regions of minima are present in each of the plots because the absolute value of the analytical solution was used when calculating each residual. Only the minima which correspond to a positive reflection coefficient are considered as valid because it is assumed that the sediment has a greater characteristic impedance than the seawater.

A slight frequency dependence in the parameter space search is observed. Generally, the minima for the higher frequency bands move upward and to the left in the parameter space (lower density, higher sound speed) while lower frequency bands have a minima nearer to the bottom right (higher density, lower sound speed). If the dataset lacks a variety of incident angles, the minimum residual can settle towards non-physical parameter values. This is because the analytical solution has little variation at these non-physical values when the angle of incidence is relatively constant. Thus, it is important to sample over a wide range of incident angles.

Site #3 has a broad range of incident angles, nearly 50 degrees, and resolves a local minima in the prescribed parameter space at each studied

frequency band. Site #1 also resolves a local minima in each frequency band, but the structure has a sweeping tapered shape. This is likely due to the comparatively narrow range of input angles of 30 degrees. The minima are used to provide density and sound speed ratio estimates, shown in Tables 4.5 and 4.6.

Results from the parameter space search provided decent estimates of ground truth. Density estimates ranged from 1.19 to 1.93 g/cm^3 and sound speed ratio estimates ranged from 0.86 to 1.14. The ground truth measurements for sediment density were between 1.63 and 1.71 g/cm^3 and an SSR slightly greater than 1.0. Error contours were used to quantify an area around the residual minima which enclosed the ground truth values. The contours are defined by a percentage value relative to the magnitude of the minima. High error contour percentage numbers can mean a few things. Either the estimate is far from ground truth, the minima is deeply set and well established, or a combination of the two. Estimates from the 10-15 kHz frequency band most closely resembled ground truth at each site and it had the smallest error contour of all site #3 results. The 10-15 kHz bandwidth estimated an average density of 1.59 g/cm^3 and an SSR near 1.0.

The average BL, FWHM, and ratio of HWHM are provided in Tables 4.7, 4.8, and 4.9. The average BL numbers are more consistent from band to band compared with the SBCE results. There was no narrowband noise artificially boosting the return and the result is a more uniform bottom loss for all frequencies. The FWHM behaves as expected with the largest bandwidth

resulting in the smallest FWHM. Three of the six bands of interest have a bandwidth of 5 kHz. Two of them have very similar FWHM values, but the 5-10 kHz bandwidth is consistently high. This might be attributable to non-uniformity in the frequency response of the measurement system. The ratio of HWHM seems to counter the FWHM. Larger bandwidths result in smaller FWHM and larger ratio of HWHM, and vice versa. This trend was observed in both the DISL and SBCE data.

The coefficients of variation were lowest at site #2 for all metrics. This is attributed to that site's data all being gathered at near-normal incidence whereas the other sites had a combination of near-normal and oblique incidence data. This site also had the least amount of total collected data which could limit variation. Lastly, site #2 is near the edge of Petit Bois Pass where the currents are not strong. The result is higher mud content and a more uniform sediment.

Near-normal incidence data was collected at each site. The bottom loss measurements from these data were used to calculate an IOI for each site, and the regression equations were used to produce Table 4.10. The regression underestimated density by nearly 10% and overestimated porosity by 7%. Interestingly, the SBCE data also underestimated density by 10%. The ground truth sound speed ratio was expected to be overestimated by regression analysis, but it was not. Instead the SSR was underestimated by nearly 5%. The trend of decreasing SSR and density with increasing porosity from site #1 to site #2 was observed in the bottom loss analysis and the ground truth

data. Site #1 was near the center of Petit Bois Pass where stronger currents led to a more sandy bottom.

Four types of benthic infauna were identified during the DISL experiment and characterized based on body type and sediment interaction type.[65] They are hard-bodied mixing, soft-bodied mixing, soft-bodied hard tube structuring, and soft-bodied soft tube structuring. Site #1 was sandier than other sites and the hard tube structuring worms were found there in abundance, over eight times the amount that was found at site #2. These hard tube structuring worms live in environments with flowing water as it carries food over their habitat. Lee et al. discusses the possibility of the tube structures causing turbulence at the boundary layer, leading to increased erosion of small silt and clay particles on the surface while maintaining a muddy layer below.[68] The presence of these organisms, and the hydrodynamic environments they reside in, could both result in higher sound speeds.

The porosity of a sediment is expected to increase when mixing infauna are present. Ground truth data compared porosity with total biomass but did not differentiate between the type of body or sediment activity. Ground truth porosity increased from 55% at site #1 to 64% at site #2. The same trend is observed in the porosity values estimated from bottom loss measurements. Porosity at site #2 is greater than both of the other sites by 2-5%. At site #3, the sediment properties are more attributable to sediment transport phenomena rather than bioturbation. The site is near the tip of Petit Bois Island in an area with a sparse presence of infauna and water current patterns similar

to site #2, allowing silt and clay particles to accumulate.

The wavelengths used to develop the regression equations for mean grain size were approximately 0.4 mm. The largest wavelength used in the DISL experiment was nearly two orders of magnitude larger that that, 0.3 m. It is not surprising that long wavelengths aren't interacting to small micron sized particles in the same way as a 400 kHz wave. The mean grain size is not able to be accurately determined at the low to mid frequencies through the application of IOI regression equations.

5.3 Conclusion

This thesis provides the background knowledge necessary to process acoustic bottom loss measurements for the purposes of marine sediment characterization and presented multiple methods for physical interpretation. A brief history of sediment characterization provided context for how technology has advanced and enabled the remote study of the seafloor. Motivation was provided for the use and application of such measurement techniques.

Ground truth measurements generally require the sediment to be removed from its natural environment and transported to a testing facility to be measured. Those who have conducted core and grab samples will attest to the fact that the process is violent and can disturb the sediment sample and affect its physical properties. Also, maintaining the temperature and hydrostatic pressure through transportation and testing is usually not possible. For this reason we seek methods, such as remote acoustic sensing, to obtain estimates

of physical properties in a non-intrusive manner.

Sediment reflection models and geoacoustic models used for sediment characterization were addressed in Chapter 3. Three major sediment representations were considered and it was decided that a fluid representation was adequate for use because of the slowness of shear waves in unconsolidated fine-grain sediments like mud. Empirical relations were introduced as a method for translating acoustic measurement into estimates of physical properties. The index of impedance regression equations were chosen because of their ability to estimate physical properties using only normal incidence echo soundings.

Chapter 4 described two sediment characterization experiments, SBCE and DISL. The echo sounder hardware, NIRMS, was introduced along with the data processing method used to analyze the acoustic data. Unique challenges were encountered when analyzing each experiment's data. The SBCE data had issues exceeding the dynamic range of the data acquisition system as the echo sounder was lowered to depth. Fortunately, three sections of data were found in which the direct path signal did not exceed the dynamic range of the system. This occurred while the device was suspended at a 60 meter altitude, satisfying the assumption of near-normal incidence. The final hurdle with the SBCE data was ship noise from the R/V Armstrong. This was overcome by bandpassing the data in six different ways and analyzing each band of interest independently. The noise mostly affected the lower bands, especially the 5-10 kHz band. Other bands provided good estimates of bottom loss, although the noise may have slightly boosted the average bottom return in any bandwidth

whose lower cutoff was set to 5 kHz.

The DISL dataset also had unique challenges to overcome. The depth of the water column was approximately 10-15 meters and often the NIRMS device was operated very near the sediment interface. It was necessary to remove the direct path signal from the matched filter output in order to separate the bottom loss data from the sidelobes of the direct path. Further, much of the data could not be assumed to be taken at near-normal incidence. Thus, a simple parameter space search was used to invert for sound speed and density, independent of incident angle.

The bottom loss values calculated from the SBCE dataset are fairly large. This could indicate that the clay particles in the mud had a "card house" flocculation structure which greatly increases porosity. Also, some amount of loss is likely unaccounted for; biological effects, surface roughness, sediment volume attenuation, gradients, poroelastic effects, etc. Because the mud is so porous, and has a fluid-like consistency, the surface roughness and poroelastic effects are assumed negligible. The biological abundance and impedance gradients measured in the area likely contributed to scattering and attenuation which are not modeled in a simple two-fluid system.

The FWHM and ratio of HWHM metrics showed similar frequency dependent trends in both the SBCE and DISL data. The difference between the two experiments was the variability of the two metrics. There are no obvious trends in the acoustic data to support reasoning for why the FWHM CV is different from one site to another, or between experiments. One possible

reason could be a difference in mud content. Model simulations presented in [2] showed that in a sandy environment, the addition of mud increased the variability of FWHM.

The DISL bottom loss numbers indicate a muddy sediment with site averaged bottom loss values ranging from 11.8 to 15.4 dB, depending upon frequency. Those values include data collected over all available incident angles, 5 to 55 degrees. Tables 4.7, 4.8, and 4.9 show that the BL, FWHM, and ratio of HWHM metrics calculated for DISL sites #1 and #3 had higher coefficients of variation than site #2. Site #2 was located in an area with slower moving currents which can sustain a more uniform sediment. Also, measurements at this site were taken only at near-normal incidence, which can reduce variation. The CV from site #2 is similar to those found in the SBCE results.

The parameter space search method is a useful tool for analyzing oblique incidence data. Improvement in the analytical model used in the search space could improve results. The effective density fluid model may be a natural extension as a method of introducing poroelastic effects. This could help to explain the slight underestimation of density shown in Tables 4.5 and 4.6. However, doing so requires estimating unknown values of Biot-Stoll parameters or using handbook values.

The IOI regressions were developed at 400 kHz and corrections have not yet been developed for data collected at low and mid frequency, 5-20 kHz. It was predicted in Section 3.5.2 that the values of sediment sound speed, porosity, and mean grain size would be overestimated, and that the

values of sediment density would be underestimated when compared to ground truth. This prediction was proven to be mostly true after results from the two experiments were processed.

Those data collected at near-normal incidence were applied to the regression equations to get estimates of geophysical parameters. In both the SBCE and DISL experiments, data collected at 5-20 kHz resulted in density estimates that underestimated ground truth by nearly 10%. The sound speed estimates for both SBCE and DISL were close to ground truth measurement and not overestimated. One could argue that they might have been slightly underestimated, counter to the predicted behavior in Section 3.5.2. The porosity and mean grain size estimates were both larger than ground truth. However, the ground truth measurements for porosity provided very large ranges which made comparison difficult. SBCE ground truth measured anywhere from 60% to 90% porosity. The mean grain size did not accurately predict ground truth values for either SBCE or DISL. In both studies, the regression had underestimated the mean grain diameter by an order of magnitude. It is clear that IOI regression equations generally aren't suitable for use with low frequency data, especially when estimating mean grain size.

The effect of benthos on the variability of bottom loss measurements was discussed in the previous sections and is a developing field of study. Improvements in sediment characterization models can be made by considering the effects of infauna on bottom loss measurements and the sediment properties. Those effects depend on knowledge of biological abundance, body type,

and activity type. Difficulty exists in pinpointing those effects and isolating how they contribute to acoustic loss mechanisms like volume scattering, gradients, and surface roughness. Biologically enhanced corrections would be a welcome improvement to current sediment characterization models.

Appendices

Appendix A

Bottom Loss Plots

A.1 SBCE

Each figure contains three plots which represent the three datasets that were isolated from cast #1 and #2. The top plot corresponds to dataset #1, the middle plot shows dataset #2, and the bottom plot shows dataset #3. All of these data are taken at near-normal incidence and the bottom return is shown near the 57 or 67 meter range. The range window on the plot is zoomed to show the bottom reflection. The data is normalized to the direct path signal and corrected for geometrical spreading loss. The oscillatory pattern of the bottom return is attributable to heave of the ship and CTD.

Figures A.2, and A.3 are obstructed by ship noise to a varied degree. The noise is audible in audio playback and sounds like a gearbox or electric motor being used to steady the heading of the ship. The result was an increase in bottom reflection return in the frequency bands where the ship noise was observed. Also, a secondary low-mid frequency active sonar was operating in the area during the experiment. This manifests in the plots as thin vertical red lines. The bottom loss values affected by interference with this sonar were discarded.

For those data which aren't saturated with noise, we observe sub-bottom returns which are correlated with the shape of the sediment interface. Some of those sub-bottom returns appear like a cascade of multiple returns in ways that can't be explained as temporal side lobes. One possible explanation is the existence of an impedance gradient in the sediment. A gradient due to compaction in the flocculation pattern of clay particles may occur with depth, allowing for some of the interface penetrating acoustic energy to become reflected in the sediment volume. Also, bioturbation processes like burrowing can restructure the surficial sediment, contributing to the gradient.

The FWHM manifests itself in these plots as the width of the bottom return reflection. Thin and well defined interface reflections are seen in those bands of interest which had a large bandwidth, and vice versa. The ratio of HWHM is not easily observable by eye.

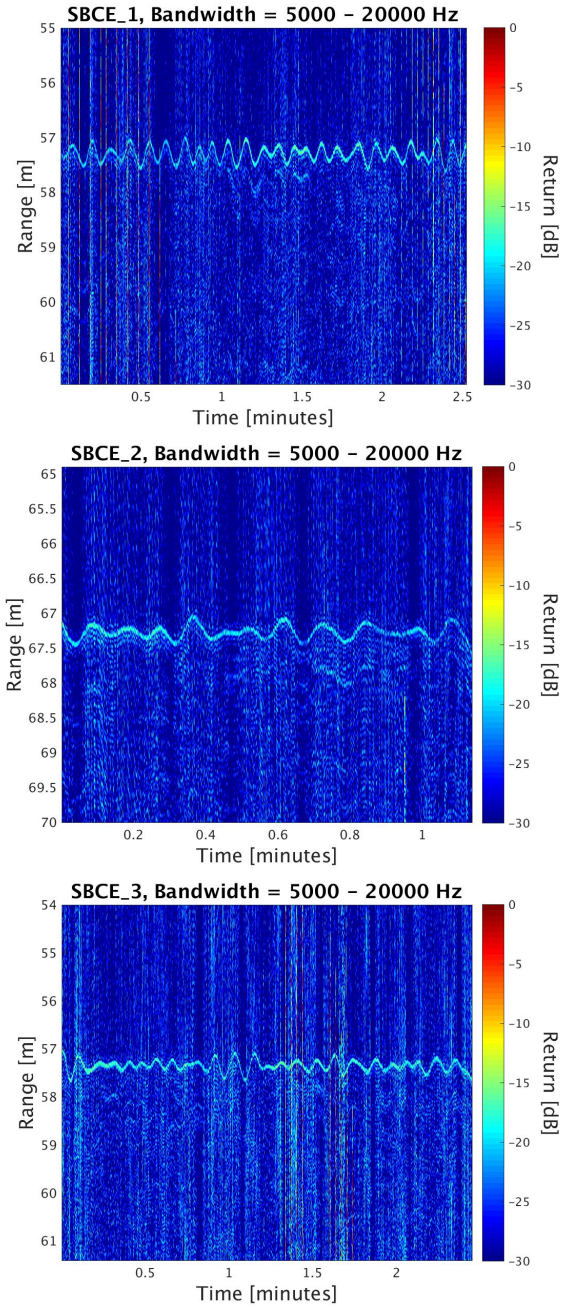

Figure A.1: SBCE bottom loss data, bandwidth = 5-20 kHz.

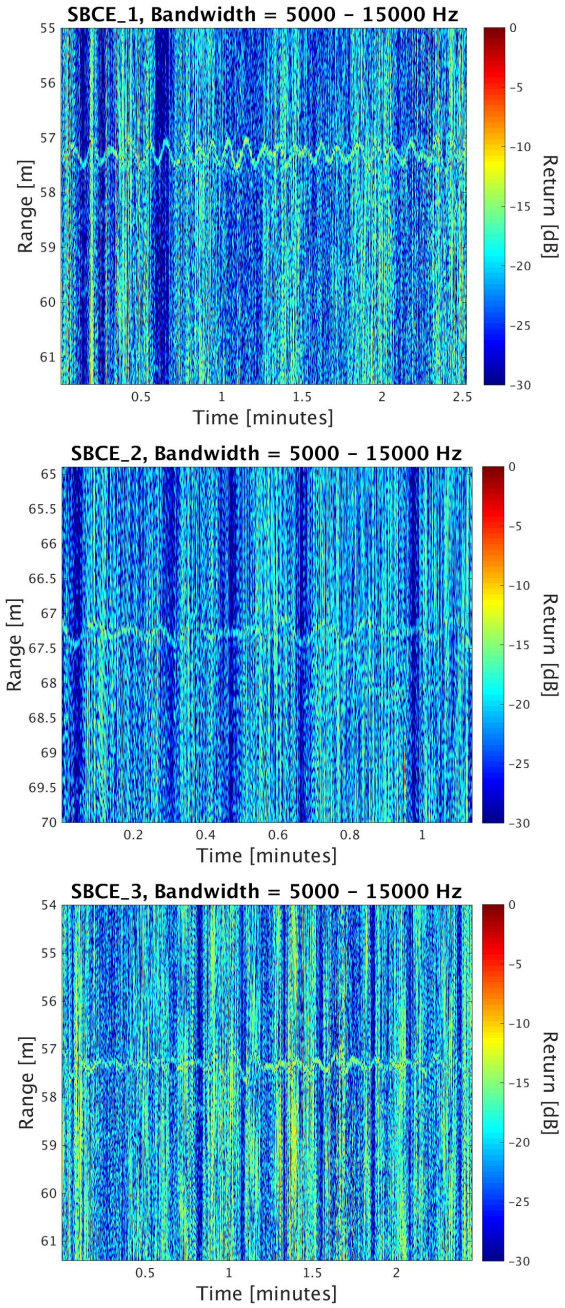

Figure A.2: SBCE bottom loss data, bandwidth = 5-15 kHz. Ship noise is clearly visible in this frequency band.

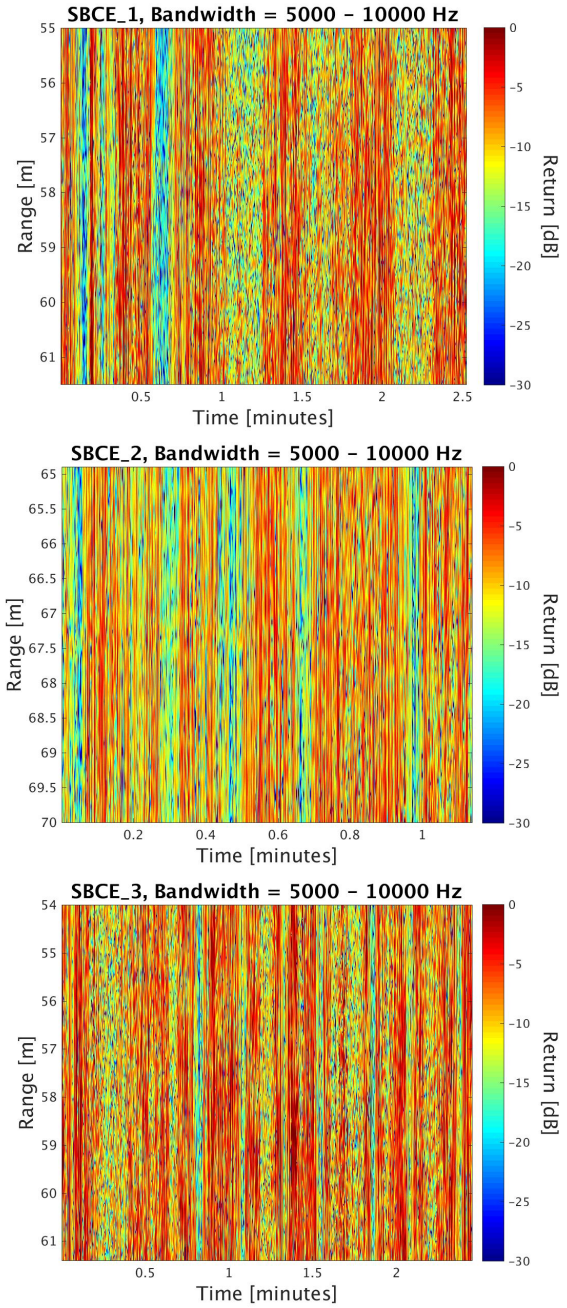

Figure A.3: SBCE bottom loss data, bandwidth = 5-10 kHz. Ship noise is clearly visible in this frequency band.

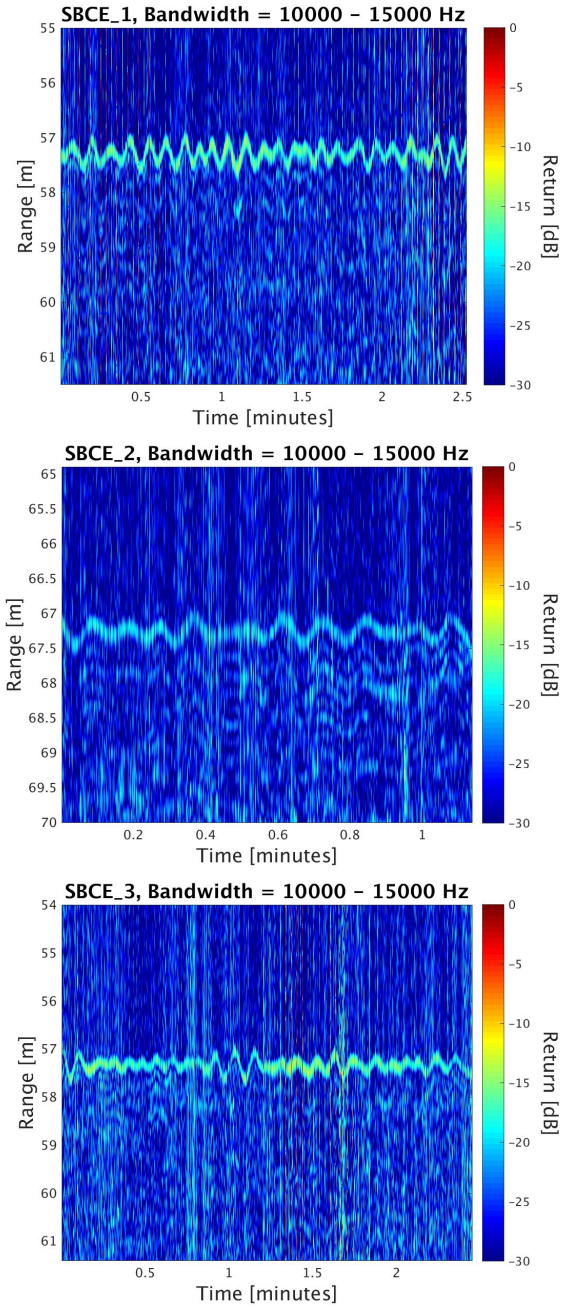

Figure A.4: SBCE bottom loss data, bandwidth = 10-15 kHz.

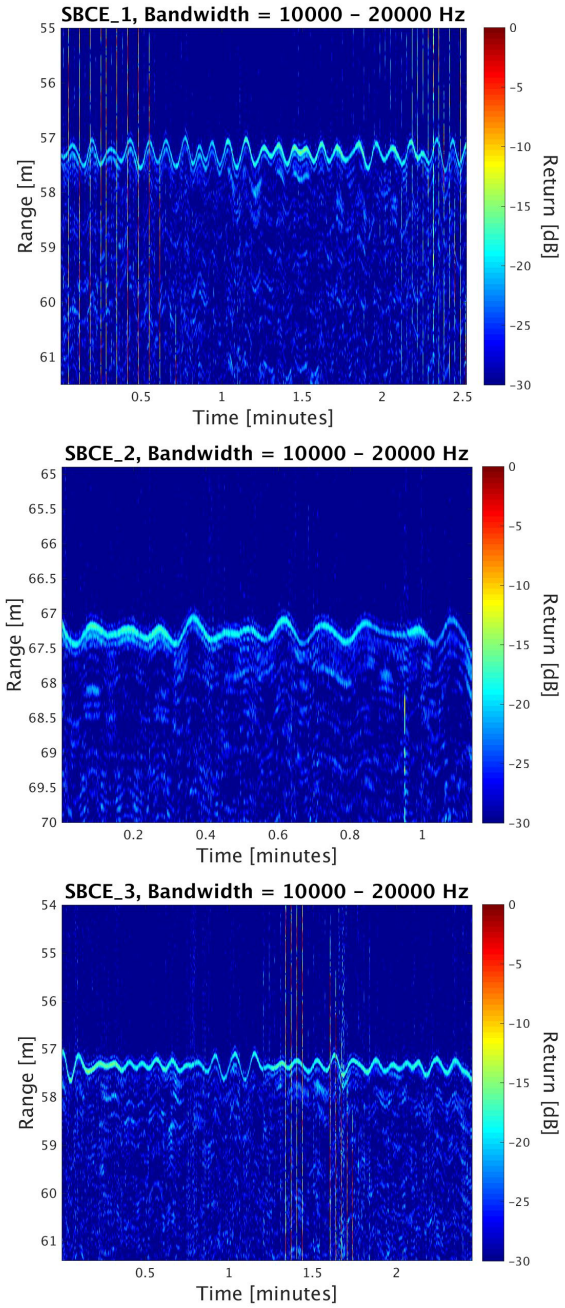

Figure A.5: SBCE bottom loss data, bandwidth = 10-20 kHz.

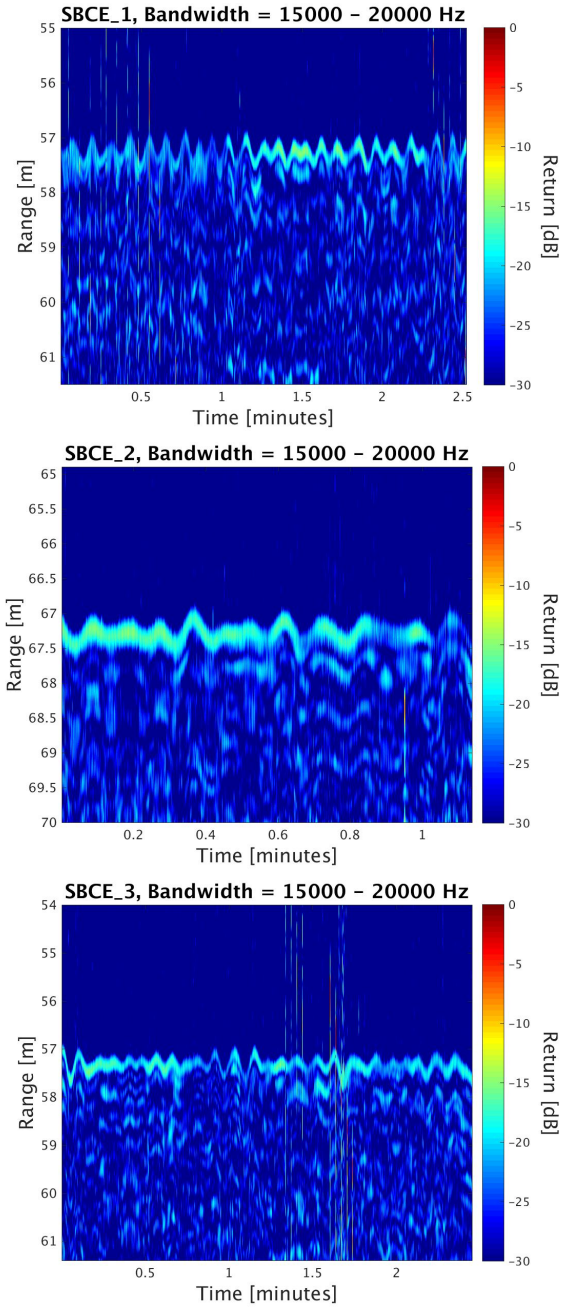

Figure A.6: SBCE bottom loss data, bandwidth = 15-20 kHz.

A.2 DISL

Each figure contains three plots which represent one cast from each of the three DISL sites. The top plot corresponds to a cast conducted at site #1, the middle plot shows data from a cast at site #2, and the bottom plot shows data from a cast at site #3. The bottom return appears near the 4 meter range. These plots represent nearly 10% of the total DISL data. The return seen at 2 meters is the surface reflection, and at the 6 meter range is the multipath return. These data sets were gathered at the shallowest incident angles, 5-7 degrees.

The sub-bottom structure observed in the SBCE data are generally not seen in the DISL data. Instead, the late energy is more randomized and uncorrelated with the shape of the interface. This may indicate that the sharp surficial density gradients observed in the New England Mud Patch aren't as prevalent in Petit Bois Pass. Only by close inspection can it be seen that site #1 has slightly more structure than sites #2 or #3. The soft-body hard-tube structuring worms were abundant at site #1 and their presence may be influencing the volume scattering.

An inquisitive eye might see Figure A.9 and notice some extra lines of high magnitude return. The low frequency matched filter template resulted in a significant late side lobe. The sidelobe of the surface reflection approaches the main lobe of the bottom reflection. The side lobe of the bottom reflection poses as a pseudo sub-layer below that. This can be corrected in future processing efforts.

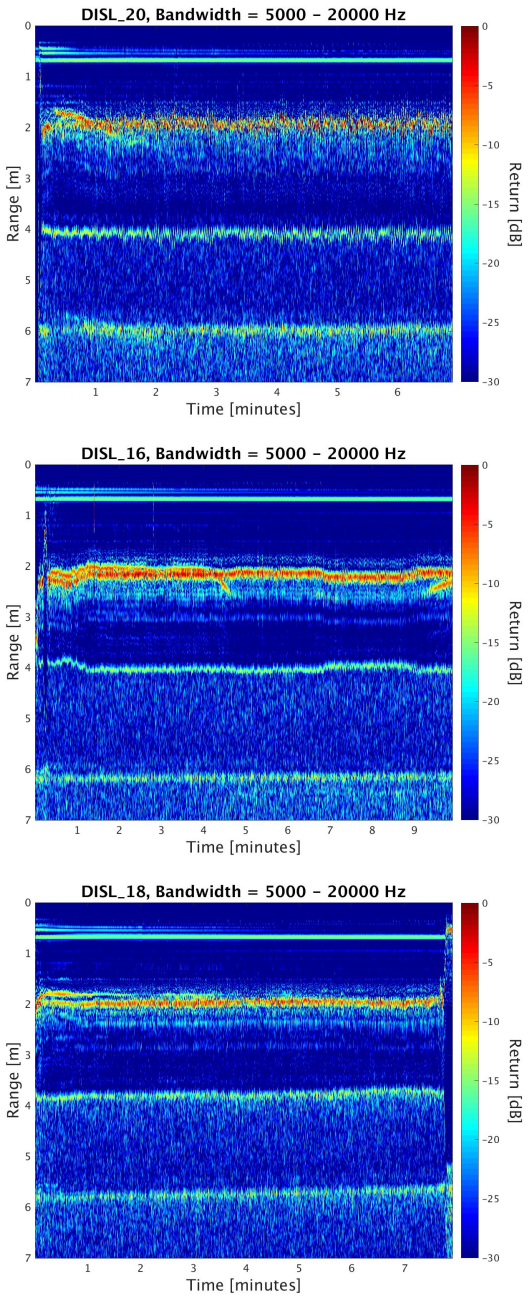

Figure A.7: DISL bottom loss data, bandwidth = 5-20 kHz.

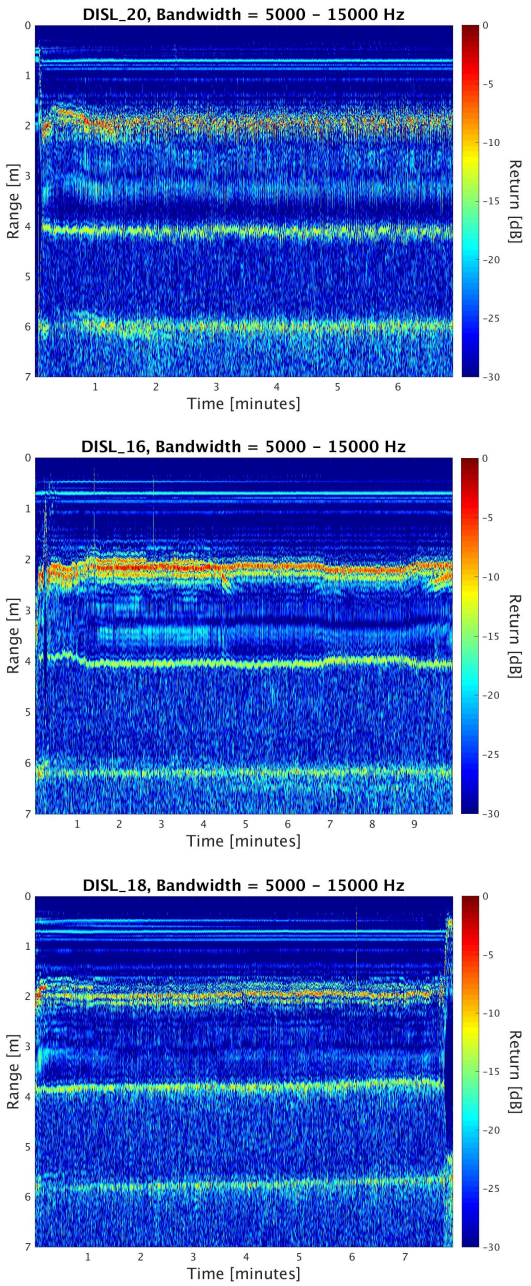

Figure A.8: DISL bottom loss data, bandwidth = 5-15 kHz.

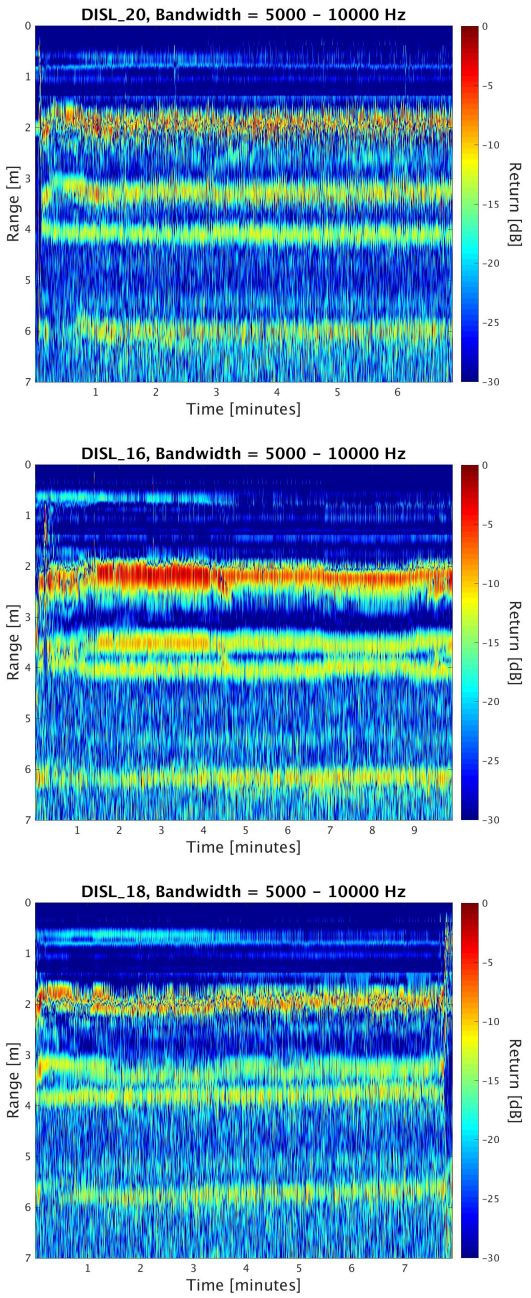

Figure A.9: DISL bottom loss data, bandwidth = 5-10 kHz.

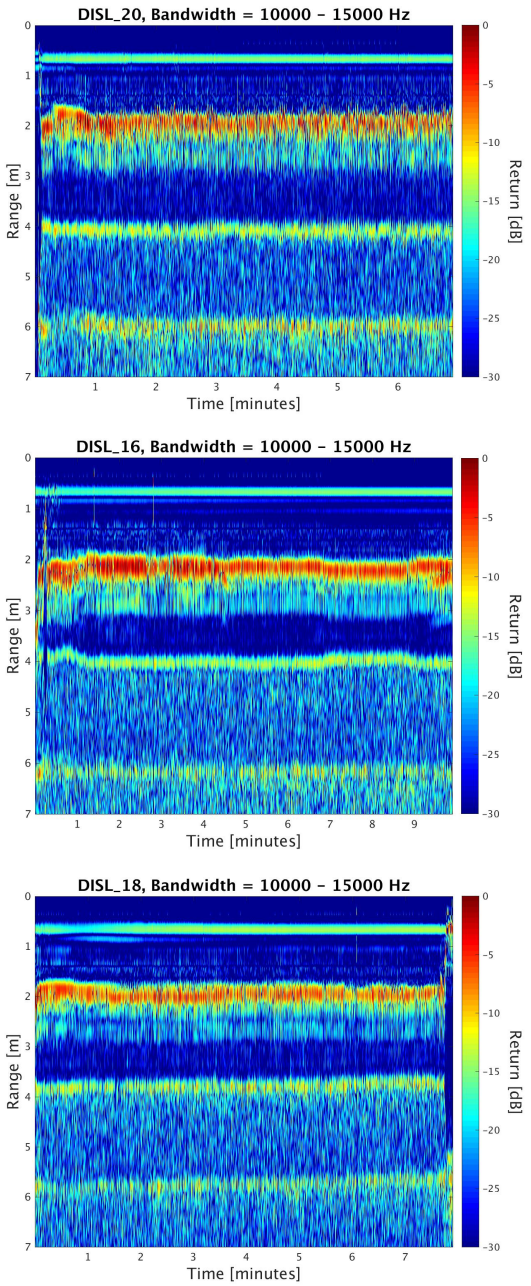

Figure A.10: DISL bottom loss data, bandwidth = 10-15 kHz.

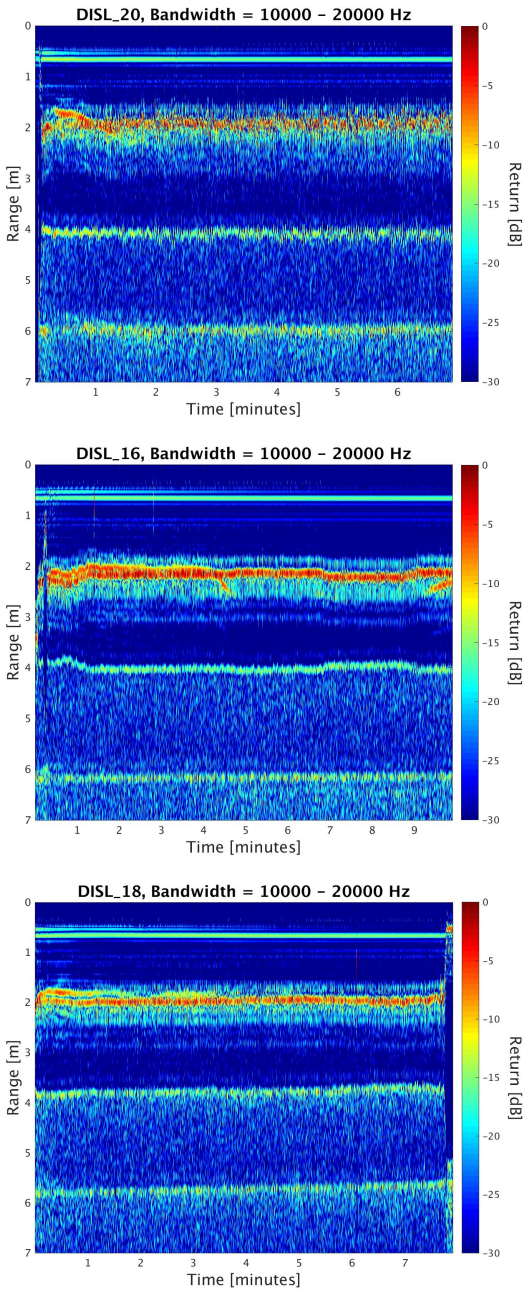

Figure A.11: DISL bottom loss data, bandwidth = 10-20 kHz.

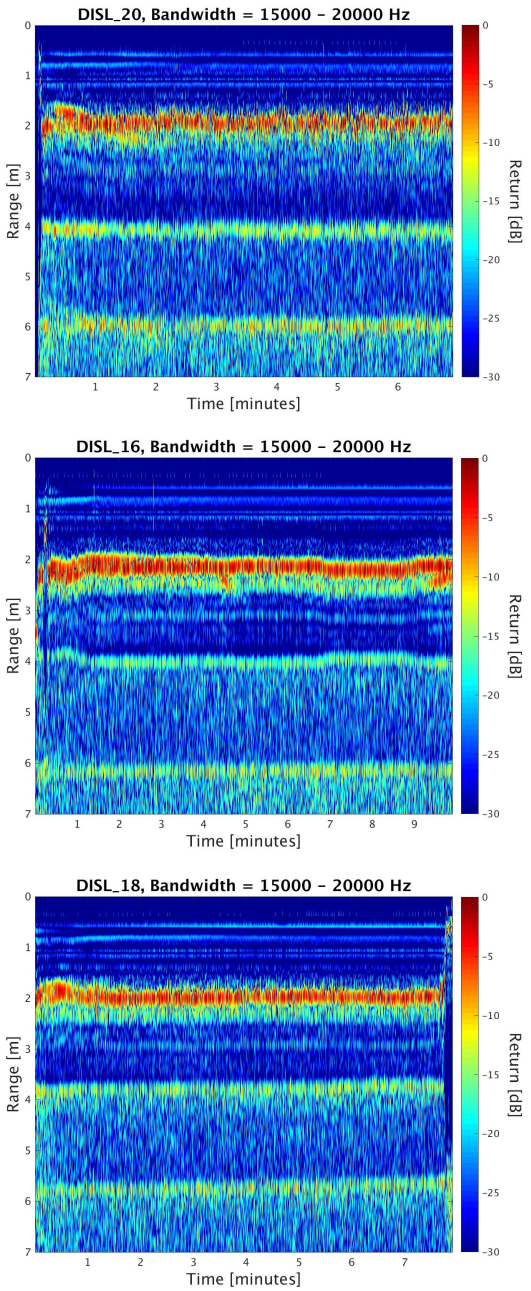

Figure A.12: DISL bottom loss data, bandwidth = 15-20 kHz.

Appendix B

Transducer Product Sheets

Model ITC-1032

Deep Water Omnidirectional Transducer

Model ITC-1032

The Model ITC-1032 spherical transducer offers broadband omnidirectional transmitting and receiving response with efficiencies of over 50%. This transducer is fabricated of Channelite-5400 lead zirconate titanate ceramic and is particularly well suited for noise sources as a broadband hydrophone and applications where an omnidirectional response is required.

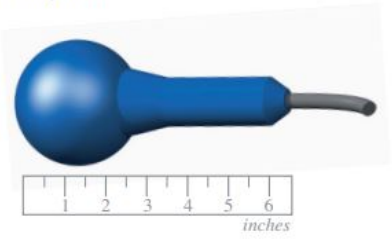

Specifications (Nominal)

Type	Projector/Hydrophone
Resonance Frequency f_r	33 kHz
Depth	1250 meters
Envelope Dimensions (in.)	2.7D
TVR at f_r	149 dB//µPa/V@1m
Midband OCV	-194 dB//1V/µPa
Suggested Band	.01 - 50 kHz
Beam Type	Spherical
Input Power	800 watts

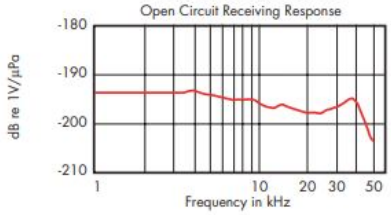

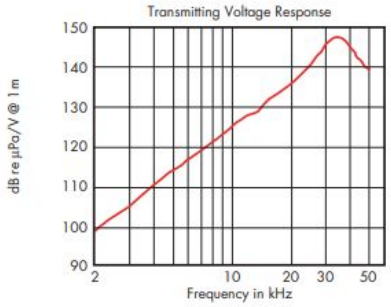

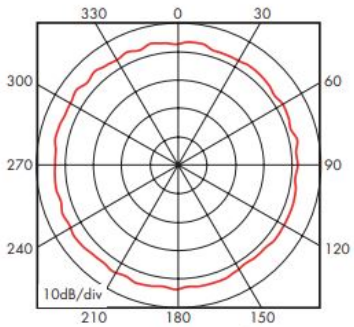

Directivity Pattern at 10.0 kHz

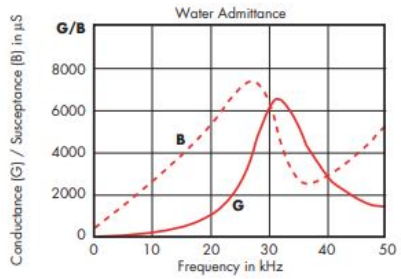

International Transducer Corporation
869 Ward Drive, Santa Barbara, CA 93111
805.683.2575 • 805.967.8199 FAX
ww.itc-transducers.com

Wilcoxon Research

Model H507A
Ultra low noise wide band hydrophone

The H507A wide band (10 Hz to 100 kHz) hydrophone is a very small high sensitivity device incorporating an ultra-low noise preamplifier (-166 dB re 1V/√Hz at 10 kHz) and a circuit for the insertion of an electrical calibration signal. In addition the preamplifier can drive up to 200 meters of cable. The sensor and amplifier are electrostatically shielded and molded in hydrolytically stable, void free polyurethane.

Dynamic

Sensitivity, referred to input	−188 dB re 1 V/µPa
Frequency range, ±3 dB	10 to 100,000 Hz
Gain[1]	10 dB
Patterns:	
XY plane, nondirectional	±1 dB to 100 kHz
XZ or YZ plane, nondirectional	±1 dB to 10 kHz
XZ or YZ plane, nondirectional over 270° span (attenuation in direction of cable exit)	±1.5 dB to 100 kHz
Acceleration sensitivity, re 1 µPa/g, 10 Hz	162 dB
Noise, re 1 µPa/√Hz:	
1 kHz	31 dB
10 kHz	22 dB
100 kHz	18 dB

Electrical

Supply voltage	18 - 24 VDC
Bias output voltage, nominal	10 VDC
Supply current	4 - 10 mA
Maximum output	3 V rms
Output impedance	50 Ω
Calibration pad	−14 dB, 40 Ω & 10 Ω 0.1W, 1 VAC rms max. input

Environmental

Operating depth	500 meters
Maximum depth	1000 meters
Maximum cable length, operation to 100 kHz	200 meters

Physical [2, 3]

Cable	10 ft., 5 conductor plus shield, stripped & tinned
External material	polyurethane

Pin	Color	Function
1	shield	case ground
2	black	signal return, common
3	red	+24 VDC
4	green	calibration input
5	white	signal output
6	yellow	not used, open

Notes: [1] Gain will vary as a function of crystal capacitance.
[2] Connectors are available with plastic or metal male locking sleeves. Please specify at time of order.
[3] Customer specified length.

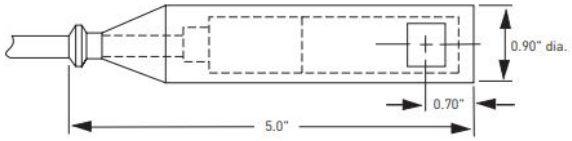

Export Classification: USML XI (c)

Wilcoxon Research Inc
21 Firstfield Rd
Gaithersburg, MD 20878
USA

Tel: 301 330 8811
Fax: 301 330 8873
Email: sensors@wilcoxon.com

www.meggitt.com

MEGGiTT
smart engineering for extreme environments

98413 Rev. B.3 01/06

Bibliography

[1] E. L. Hamilton, "Geoacoustic modeling of the sea floor," *J. Acoust. Soc. Am.*, vol. 68, no. 5, pp. 1313–1340, 1980.

[2] M. J. Isakson, J. N. Piper, and A. R. McNeese, "Measurements, metrics, and modeling of normal-incidence acoustic interaction with ocean sediment," *IEEE J. Oceanic Eng.*, vol. 44, no. 4, pp. 956–971, 2019.

[3] J. T. Anderson, D. Van Holliday, R. Kloser, D. Reid, Y. Simard, C. Brown, R. Chapman, R. Coggan, R. Kieser, W. Michaels, A. Orlowski, J. Preston, E. J. Simmonds, and A. Stepnowski, *Acoustic Seabed Classification of Marine Physical and Biological Landscapes*. International Council for the Exploration of the Sea, 2007.

[4] H. A. Karl, J. L. Chin, E. Ueber, P. H. Stauffer, and J. W. Hendley, *Beyond the Golden Gate: Oceanography, Geology, Biology, and Environmental Issues in the Gulf of the Farallones*. U.S. Dept. of the Interior, U.S. Geological Survey, Virginia, 2001.

[5] A. E. Theberge, "Sounding pole to sea beam," in *Technical Papers 1989 ASPRS/ACSM Annual Convention Surveying and Cartography*, vol. 5, pp. 334–346, NOAA Central Library Call No. TA501.A638, 1989.

[6] M. Allaby, *Oceans: A Scientific History of Oceans and Marine Life*. Infobase Publishing, 2009.

[7] S. Höhler, "Depth records and ocean volumes: ocean profiling by sounding technology, 1850-1930," *Hist. Technol.*, vol. 18, no. 2, pp. 119–154, 2002.

[8] J. T. Dubin, "Sediment characterization using in situ measurements of acoustic properties," Master's thesis, The University of Texas at Austin, 2018.

[9] E. L. Hamilton, "Prediction of deep-sea sediment properties: state-of-the-art," in *Deep-Sea Sediments*, pp. 1–43, Springer, 1974.

[10] G. R. Venegas, P. S. Wilson, K. M. Lee, M. S. Ballard, A. R. McNeese, and K. M. Dorgan, "Core and resonance logger measurements of fine-grained sediments containing infauna," *Proc. Mtgs. Acoust.*, vol. 31, no. 005001, 2017.

[11] R. H. Plumb Jr., "Procedures for handling and chemical analysis of sediment and water samples," tech. rep., State University College at Buffalo, Great Lakes Laboratory, 1981.

[12] M. Snellen, K. Siemes, and D. G. Simons, "Model-based sediment classification using single-beam echosounder signals," *J. Acoust. Soc. Am.*, vol. 129, no. 5, pp. 2878–2888, 2011.

[13] P. A. V. Walree, M. A. Ainslie, and D. G. Simons, "Mean grain size mapping with single-beam echo sounders," *J. Acoust. Soc. Am.*, vol. 120, no. 5, pp. 2555–2566, 2006.

[14] L. Lu, Q. Ren, L. Ma, S. Guo, and T. Liao, "Sediment acoustic characterization by optimizing single-beam sonar echoes," in *2017 IEEE International Conference on Signal Processing, Communications and Computing (ICSPCC)*, 2017.

[15] B. E. Tucholke and D. J. Shirley, "Comparison of laboratory and in situ compressional-wave velocity measurements on sediment cores from the western north atlantic," *J. Geophys. Res. Solid Earth*, vol. 84, no. B2, pp. 687–695, 1979.

[16] M. S. Ballard, K. M. Lee, A. R. McNeese, P. S. Wilson, J. D. Chaytor, J. A. Goff, and A. H. Reed, "In situ measurements of compressional wave speed during gravity coring operations in the new england mud patch," *IEEE J. Oceanic Eng.*, pp. 1–13, 2019.

[17] J. T. Anderson, D. Van Holliday, R. Kloser, D. G. Reid, and Y. Simard, "Acoustic seabed classification: current practice and future directions," *ICES J. Mar. Sci.*, vol. 65, pp. 1004–1011, 04 2008.

[18] D. D. Sternlicht and C. P. de Moustier, "Time-dependent seafloor acoustic backscatter (10-100 kHz)," *J. Acoust. Soc. Am.*, vol. 114, no. 5, pp. 2709–2725, 2003.

[19] R. T. Bachman, "Acoustic and physical property relationships in marine sediment," *J. Acoust. Soc. Am.*, vol. 78, no. 2, pp. 616–621, 1985.

[20] E. L. Hamilton, "Reflection coefficients and bottom losses at normal incidence computed from pacific sediment properties," *J. Geophys.*, vol. 35, no. 6, pp. 995–1004, 1970.

[21] D. D. Sternlicht and C. P. de Moustier, "Remote sensing of sediment characteristics by optimized echo-envelope matching," *J. Acoust. Soc. Am.*, vol. 114, no. 5, pp. 2727–2743, 2003.

[22] M. M. Harris, W. E. Avera, A. Abelev, F. W. Bentrem, and L. D. Bibee, "Sensing shallow seafloor and sediment properties, recent history," in *Oceans 2008*, 2008.

[23] C. J. Brown, S. J. Smith, P. Lawton, and J. T. Anderson, "Benthic habitat mapping: A review of progress towards improved understanding of the spatial ecology of the seafloor using acoustic techniques," *Estuarine Coastal Shelf Sci.*, vol. 92, no. 3, pp. 502–520, 2011.

[24] O. Gazi, *Understanding Digital Signal Processing.* Springer, Singapore, 2018.

[25] R. G. Lyons, *Understanding Digital Signal Processing.* Pearson Education, Inc, 3 ed., 2011.

[26] B. R. Mahafza, *Introduction to Radar Analysis.* CRC Press, Taylor and Francis Group, Boca Raton, 2017.

[27] J. R. Klauder, A. C. Price, S. Darlington, and W. J. Albersheim, "The theory and design of chirp radars," *The Bell System Technical Journal*, vol. 39, no. 4, pp. 745–808, 1960.

[28] W. Van Etten, *Introduction to Random Signals and Noise*. Wiley Online Library, 2005.

[29] C. E. Cook and M. Bernfeld, *Radar Signals: An Introduction to Theory and Application*. Elsevier, 1967.

[30] V. Y. Bouniakowsky, "Sur quelques inequalités concernant les intégrales aux differences finis," *Mem. Acad. Sci. St. Peterbourg*, vol. 7, no. 1, pp. 3–4, 1859.

[31] C. E. Cook, "Pulse compression-key to more efficient radar transmission," in *Proceedings of the IRE*, vol. 48, pp. 310–316, Institute of Radio Engineers, March 1960.

[32] C. H. Ma, "Stepped-frequency pulse train waveforms for improved range resolution," Master's thesis, Massachusetts Institute of Technology, 1996.

[33] D. R. Jackson and M. D. Richardson, *High-frequency Seafloor Acoustics*. Springer, New York, 2011.

[34] G. E. Box and N. R. Draper, *Empirical Model-building and Response Surfaces*, vol. 424. Wiley New York, 1987.

[35] A. L. Bonomo, *An evaluation of competing geoacoustic models and their applicability to sandy ocean sediments.* PhD thesis, The University of Texas at Austin, 2017.

[36] M. A. Biot, "Theory of propagation of elastic waves in a fluidsaturated porous solid. I. Low frequency range," *J. Acoust. Soc. Am.*, vol. 28, no. 2, pp. 168–178, 1956.

[37] M. A. Biot, "Theory of propagation of elastic waves in a fluidsaturated porous solid. II. Higher frequency range," *J. Acoust. Soc. Am.*, vol. 28, no. 2, pp. 179–191, 1956.

[38] R. D. Stoll, *Sediment Acoustics.* Springer, Berlin, 1989.

[39] N. P. Chotiros, *Acoustics of the Seabed as a Poroelastic Medium.* Springer, Switzerland, 2017.

[40] K. L. Williams, "An effective density fluid model for acoustic propagation in sediments derived from Biot theory," *J. Acoust. Soc. Am.*, vol. 110, no. 5, pp. 2276–2281, 2001.

[41] L. E. Kinsler, A. R. Frey, A. B. Coppens, and J. V. Sanders, *Fundamentals of Acoustics.* Wiley, New York, 2000.

[42] D. T. Blackstock, *Fundamentals of Physical Acoustics.* Wiley, New York, 2000.

[43] A. D. Pierce, *Acoustics: An Introduction to its Physical Principles and Applications*. McGraw-Hill, 1981.

[44] L. M. Brekhovskikh, *Waves in Layered Media*. Academic Press, New York, 1980.

[45] E. L. Hamilton, G. Shumway, H. W. Menard, and C. J. Shipek, "Acoustic and other physical properties of shallow-water sediments off San Diego," *J. Acoust. Soc. Am.*, vol. 28, no. 1, pp. 1–1, 1956.

[46] G. Shumway, "Sound speed and absorption studies of marine sediments by a resonance method," *J. Geophys.*, vol. 25, no. 2, pp. 451–467, 1960.

[47] J. E. Nafe and C. L. Drake, "Physical properties of marine sediments," tech. rep., Lamont Geological Observatory Palisades, NY, 1961.

[48] A. W. Nolle, W. A. Hoyer, J. F. Mifsud, W. R. Runyan, and M. B. Ward, "Acoustical properties of water-filled sands," *J. Acoust. Soc. Am.*, vol. 35, no. 9, pp. 1394–1408, 1963.

[49] A. B. Wood and D. E. Weston, "The propagation of sound in mud," *Acta Acust. united Acust.*, vol. 14, no. 3, pp. 156–162, 1964.

[50] L. D. Hampton, "Acoustic properties of sediments," *J. Acoust. Soc. Am.*, vol. 42, no. 4, pp. 882–890, 1967.

[51] K. V. Mackenzie, "Reflection of sound from coastal bottoms," *J. Acoust. Soc. Am.*, vol. 32, no. 2, pp. 221–231, 1960.

[52] R. J. Urick, "Side scattering of sound in shallow water," *J. Acoust. Soc. Am.*, vol. 32, no. 3, pp. 351–355, 1960.

[53] D. N. Lambert, J. C. Cranford, and D. J. Walter, "Development of a high resolution acoustic seafloor classification survey system," *Proc. Inst. Acoust.*, vol. 15, pp. 149–156, Apr 1993.

[54] M. J. Buckingham, "Wave propagation, stress relaxation, and grain-to-grain shearing in saturated, unconsolidated marine sediments," *J. Acoust. Soc. Am.*, vol. 108, no. 6, pp. 2796–2815, 2000.

[55] M. D. Richardson and K. B. Briggs, "Empirical predictions of seafloor properties based on remotely measured sediment impedance," in *AIP Conf. Proc.*, vol. 728, pp. 12–21, 2004.

[56] J. M. Hovem, M. D. Richardson, and R. D. Stoll, *Shear Waves in Marine Sediments*. Springer Science & Business Media, 2012.

[57] M. D. Richardson, "In-situ, shallow-water sediments geoacoustic properties," in *Proceedings International Conference on Shallow-Water Acoustics*, pp. 163–170, 1997.

[58] E. L. Hamilton, "Compressional wave attenuation in marine sediments," *J. Geophys.*, vol. 37, no. 4, pp. 620–646, 1972.

[59] E. L. Hamilton and R. T. Bachman, "Sound velocity and related properties of marine sediments," *J. Acoust. Soc. Am.*, vol. 72, no. 6, pp. 1891–1904, 1982.

[60] R. T. Bachman, "Estimating velocity ratio in marine sediment," *J. Acoust. Soc. Am.*, vol. 86, no. 5, pp. 2029–2032, 1989.

[61] "High-frequency ocean environmental acoustic models handbook," tech. rep., 1994. APL-UW TR-9407, Applied Physics Laboratory, University of Washington. Seattle, WA.

[62] J. Yang and D. R. Jackson, "Measurement of sound speed in fine-grained sediments during the seabed characterization experiment," *IEEE J. Oceanic Eng.*, 2019.

[63] K. M. Lee, M. S. Ballard, G. R. Venegas, P. S. Wilson, K. M. Dorgan, A. H. Reed, and E. Roosen, "Preliminary characterization of surficial sediment acoustic properties and infauna in the new england mud patch," *Proc. Mtgs. Acoust.*, vol. 26, no. 070003, 2016.

[64] D. P. Knobles and P. S. Wilson, "Seabed characterization experiment." https://wwwext.arlut.utexas.edu/sbcex/index.html.

[65] K. M. Lee, M. S. Ballard, A. R. McNeese, W. M. Ballentine, K. M. Dorgan, G. R. Venegas, and P. S. Wilson, "Comparison between infauna abundance and seabed geoacoustic properties," *J. Acoust. Soc. Am.*, vol. 142, no. 4, pp. 2693–2693, 2017.

[66] M. D. Richardson and D. K. Young, "Geoacoustic models and bioturbation," *Marine Geology*, vol. 38, no. 1, pp. 205–218, 1980.

[67] K. M. Dorgan, W. Ballentine, G. Lockridge, E. Kiskaddon, M. S. Ballard, K. M. Lee, and P. S. Wilson, "Impacts of simulated infaunal activities on acoustic wave propagation in marine sediments," *J. Acoust. Soc. Am.*, vol. 147, no. 2, pp. 812–823, 2020.

[68] K. M. Lee, G. R. Venegas, M. S. Ballard, P. S. Wilson, and K. M. Dorgan, "Acoustics of biologically active marine sediments," *Proc. Mtgs. Acoust.*, vol. 33, no. 005003, 2018.

[69] H. J. Camin and M. J. Isakson, "A comparison of sediment reflection coefficient measurements to elastic and poro-elastic models," *J. Acoust. Soc. Am.*, vol. 120, no. 5, pp. 2437–2449, 2006.

[70] L. M. Brekhovskikh and Y. P. Lysanov, *Fundamentals of Ocean Acoustics*. Springer, 3 ed., 2011.